

Analogue modelling of basin inversion: the role of oblique kinematics and implications for the Araripe Basin (Brazil)

Pâmela C. Richetti^{1,2}, Frank Zwaan^{2,3,4}, Guido Schreurs², Renata S. Schmitt^{1, 2, 5, 4}, Timothy C. Schmid²

¹ ~~Programa de Pós-graduação em Geologia-PPGL~~, Universidade Federal do Rio de Janeiro, ~~Programa de Pós-graduação em Geologia-PPGL~~, Brazil

² ~~Institute of Geological Sciences~~, University of Bern, ~~Institute of Geological Sciences~~, Bern, Switzerland

³ Helmholtz Centre Potsdam - GFZ German Research Centre for Geosciences, Potsdam, Germany

⁴ ~~University of Fribourg, Department of Geosciences, Fribourg, Switzerland~~

⁵ ~~Departamento de Geologia-IGEO~~, Universidade Federal do Rio de Janeiro, ~~Departamento de Geologia-IGEO~~, Brazil

Correspondence: Pâmela C. Richetti (pamelarichetti@geologia.ufrj.br)

Abstract.

Basin inversion is a process that takes place when a sedimentary basin is subjected to compressional stresses resulting in reactivation of pre-existing faults and/or localization of deformation along new reverse faults. The Araripe Basin (NE Brazil) is an example of a Cretaceous intracontinental aborted rift with its sedimentary infill found at ca. 1000 m altitude ~~in the present day~~. Post-rift basin inversion ~~is proposed has been proposed by previous authors~~ as the cause of this topographic high, ~~but -hH~~ ~~however~~ how inversion ~~mechanisms~~ affected this basin, ~~however, is still remains~~ a matter of debate, with two end member scenarios: reactivation of pre-existing normal faults leading to local uplift, or regional ~~tectonic~~ uplift, ~~but neither~~. ~~Neither end member fully explains the observations from seismic and field data.~~ In this study, we ~~therefore~~ conducted analogue models ~~of basin inversion~~ to ~~explore how basin inversion in the Araripe Basin could have taken place~~ ~~test these scenarios~~. We present two series of crustal-scale brittle-viscous experiments: i) ~~extension-extension~~ followed by ~~compression-compression~~ without sedimentation, with a variation of ~~in rifting divergence~~ and ~~inversion convergence~~ directions (orthogonal or 45° oblique) and ii) ~~extension-extension and followed by compression-compression~~ with syn-rift sedimentation, with the same variation in rifting and inversion directions. We ~~used~~ ~~applied~~ a seed representing a structural weakness ~~that was applied~~ at the base of the brittle layer to localize deformation along the model axis. We found that orthogonal rifting without sedimentation forms through-going ~~border-graben boundary~~ faults, whereas oblique rifting ~~initially~~ creates ~~initial en echelon~~ *échelon* faults that eventually link up creating large ~~border-graben boundary~~ faults. Rift basins with syn-rift sedimentation evolved in a similar fashion, however sedimentary loading ~~resulted in~~ increased subsidence. During ~~both oblique and orthogonal~~ inversion, most ~~deformation shortening~~ is accommodated along new ~~low-low-angle~~ reverse faults. ~~Within that framework,~~ ~~Significant~~ intra-graben fault reactivation ~~occurred~~ ~~occurred~~ in ~~all~~ models without ~~syn-rift~~ sedimentation. By contrast, ~~syn-rift sedimentation~~ ~~orthogonal inversion of models with syn-rift sedimentation did not reactivate rift faults, whereas caused~~ only minor reactivation of rift faults ~~took place in during~~ oblique

40

inversion since the sediments acted as a buffer during ~~compression~~convergence,; no rift fault reactivation occurred in orthogonal compression situations. ~~Based on these~~our modelling results. ~~Comparing the existing scenarios for inversion in the Araripe Basin with our model results and field data show that these scenarios do not fully explain the natural example. Therefore, w~~we propose an alternative scenario for basin inversion in the evolution of the Araripe Basin, based on our models, involving oblique ~~compression~~inversion and the development of ~~low~~low-angle reverse faults, which better ~~explains inversion in the Araripe Basin~~fits observations from seismic lines and field data from the region.

1 Introduction

45 The ~~tectonic~~ inversion of sedimentary basins as a result of compressional tectonics is a widely discussed topic due to its importance for the development of mineral (Sibson and Scott, 1998) and hydrocarbon deposits (Turner and Williams, 2004). Especially inverted intraplate rift basins that are currently ~~situated~~ ~~exposed~~ above sea level can play an important role for the understanding of their offshore equivalents, since they provide access to outcrops that otherwise can only be analyzed via indirect geophysical methods (e.g., Stanton et al., 2014; Rebelo et al., 2021).

50 In this context, the Araripe Basin in NE Brazil (~~Fig. 1~~), is an excellent example of an ~~exposed~~ inverted intraplate rift basin (~~Fig. 1~~). This Early Cretaceous rift basin is part of the aborted Brazilian Northeast Rift System (BNRS) (de Matos, 1992) located at the intersection of the equatorial and central segments of the South Atlantic Ocean (Moulin et al., 2010). This rift system formed within the well-developed network of NE-SW and E-W striking Precambrian ductile shear zones in the basement of the Borborema Province (Fig. 1a) (Vauchez et al., 1995; Brito Neves et al., 2000; Ganade de Araujo et al., 2014). The rift structures of the Araripe Basin ~~are mainly~~ ~~mainly~~ ~~strike~~ NE-SW ~~and E-W~~ (Fig. 1a), indicating brittle reactivation of the basement shear zones ~~during rifting~~ (de Matos, 1992), ~~especially the dextral sinistral reactivation of the E-W Patos Shear Zone bounding the north of the basin~~ (Fig. 1a). ~~However, the exact kinematics of rifting during Araripe Basin remain a matter of debate, with some authors proposing orthogonal kinematics, whereas others invoke transtension (e.g., Rosa et al. 2022).~~

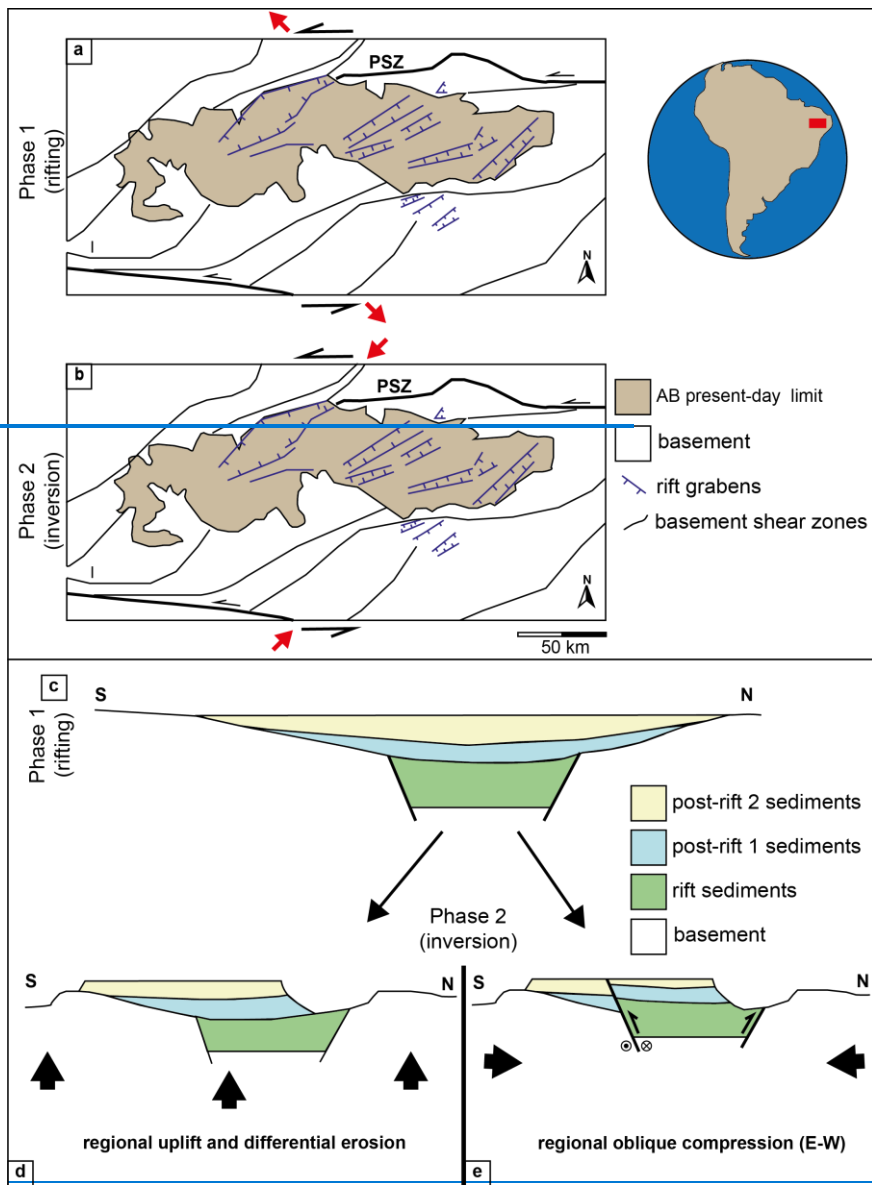
60 After rifting and subsequent thermal subsidence (Assine, 2007), the basin registered a phase of inversion (Fig. 1b) (Marques et al., 2014) and its sedimentary infill is presently situated, at its highest point, at 1000 m above sea level ~~and ca. 500 m above the surrounding basement~~. Similarly, the Borborema Province ~~generally~~ contains high topographies and evidence of recent uplift (Lamarque and Julià, 2019; Neto et al., 2019), ~~and o-~~ Other basins in the BNRS also present evidence of tectonic inversion ([Gurgel et al., 2013](#); [Nogueira et al., 2015](#); [Vasconcelos et al., 2021](#); [Bezerra et al., 2020](#); [Ramos et al., 2022](#)). In the Araripe Basin, Marques et al. (2014) proposed that inversion resulted from far-field ENE-WSW directed horizontal ~~maximum compressive~~ stress. They concluded that this deformation is consistent with the formation of new oceanic crust in the South Atlantic to the east and the development of the Andes to the west, resulting in overall compression of the South America plate ([Marques et al., 2013](#)).

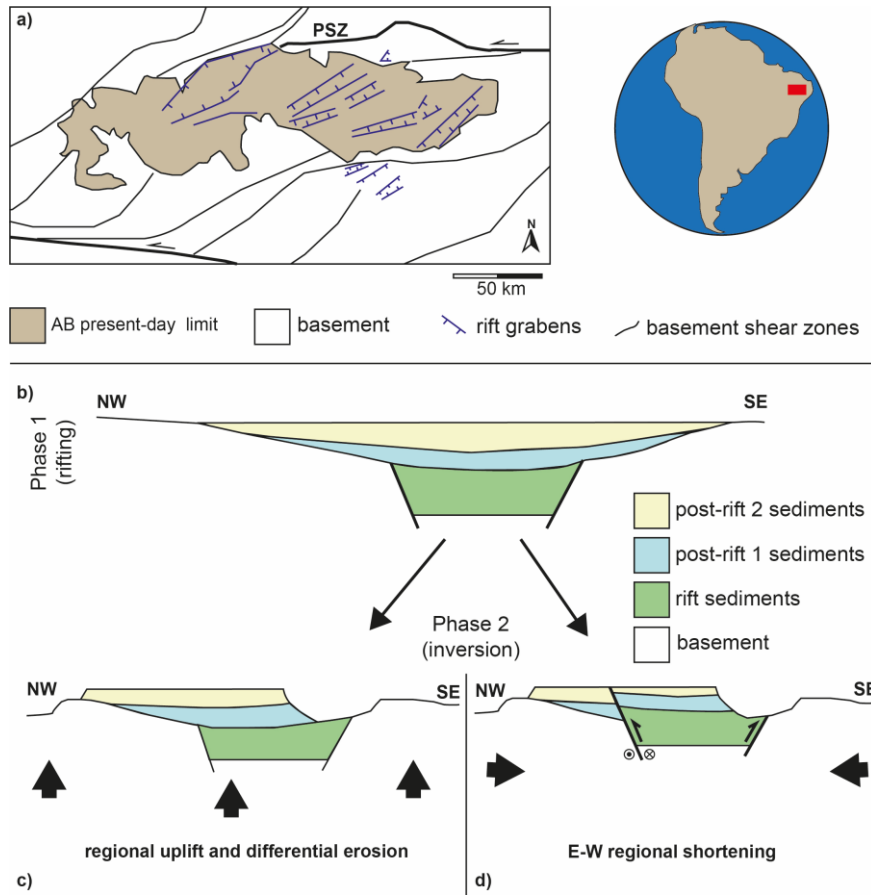
65 According to Marques et al. (2014), this compression caused ~~the complete~~ ~~large-scale~~ inversion of the initial high angle normal faults of the Araripe Basin (Fig. 1e) through ~~an~~ oblique ~~compression~~ ~~convergence~~ and injection of soft material ~~into~~ these faults. By contrast, Peulvast and Bétard, (2015) proposed that the present-day topographic elevation of the basin is due to ~~the~~ regional uplift of the Borborema Province and the action of differential erosion (Fig. 1d). ~~The Peulvast and Bétard (2015) scenario fits with the general absence of large-scale inversion of normal faults as seen on seismic sections from the Araripe Basin (Ponte and Ponte-filho, 1996, Rosa et al., 2022). However, on closer inspection, these seismic sections do in fact show a limited degree of normal fault inversion (Ponte and Ponte-filho, 1996, Rosa et al., 2022), and localized reverse faulting linked to basin inversion is observed in nearby basins of the same age as well (e.g., the Rio do Peixe Basin, Vasconcelos et al., 2021).~~ As such, the exact mechanism causing inversion, and to what degree rift structures were reactivated in the Araripe Basin remains unclear, requiring further

Formatted: Highlight

research with new approaches. One of these new approaches is the use of analogue modelling, which has shown to be a useful tool to understand the evolution of inverted basins and the mechanisms involved in various settings ([Brun and Nalpas, 1996](#); [Nalpas et al., 1995](#); [Panien et al., 2005a](#); [del Ventisette et al., 2005, 2006](#); [Marques and Nogueira, 2008](#); [Pinto et al., 2010a](#); [di Domenica et al., 2014](#); [Jara et al., 2018](#); [Zwaan et al., 2022b](#)).

In this paper we therefore present the results of new analogue modeling experiments with a novel set-up, which are aimed at evaluating ~~whether whether horizontal compression~~ tectonic compression could have indeed have caused the inversion observed in the Araripe Basin, the normal fault reactivation and full basin extrusion in the Araripe Basin as proposed by Marques et al. (2014), or whether regional uplift and differential erosion as proposed by Peulvast and Bétard (2015) forms a better explanation. In our models we test the influence of orthogonal ($\alpha=0$) or oblique ($\alpha=45^\circ$) ~~extension~~ divergence, followed by either orthogonal or oblique ~~compression~~ convergence, as well as syn-rift sedimentation on ~~rift~~ initial basin development and on subsequent inversion structures. We then compare our model results with data from the Araripe Basin nature, example in order to provide and propose an updated scenario for inversion ~~in~~ of the Araripe Basin involving oblique inversion and the development of low-angle reverse faults outside the basin. new insights on this basin compressional inversion ~~inversion models by Marques et al. (2014) and Peulvast and Bétard (2015) and propose a new interpretation of how inversion took place in the basin.~~





105 **Figure 1:** **a)** Structural geology of the study area and present-day Araripe Basin (AB). **(a)** NE-SW rift related structures (in blue) and Precambrian basement shear zones (in black), modified after Camacho and de Oliveira **E_c** Sousa (2017). PSZ: Patos Shear Zone. **b)** Inversion kinematics after Marques et al. (2014). **(b)** Schematic N-S **cross** section representing rift and **post**-post-rift formations in the Araripe Basin prior to inversion. **(c)** Schematic representation of the Araripe Basin inversion model based on regional uplift followed by differential erosion proposed by Peulvast and Bétard (2015). **(d)** Schematic representation of the Araripe Basin inversion model as a result of regional oblique **compression-convergence** proposed by Marques et al. (2014).

110

2 Methods

2.1 Model set up

115 For this study of crustal-scale basin inversion processes, we used an experimental set-up involving two long mobile sidewalls, two rubber **sidewalls-end walls** (fixed between the mobile walls, closing the short model ends), and a base consisting of a mobile and a fixed base plate (Fig. 2a). We positioned a 5 cm **high-thick** block consisting of **an intercalation-of-intercalated** foam (1 cm thick) and Plexiglas (0.5 cm thick) bars above the base plates and between the long sidewalls (Fig. 2a,b). This foam/Plexiglas block, initially 36.5 cm

120 wide, was compressed prior to adding the model materials in order to reach the initial [experiment](#)-width of
30 cm (Fig. 2a,b). [This set-up has been regularly used for orthogonal and oblique rifting, and compression
transpression models \(Schreurs and Colletta, 1998, 2002; Zwaan and Schreurs, 2017; Zwaan et al., 2016,
2018a, 2020; Schmid et al., 2022a, b\). The 4D](#)divergence of the mobile [long](#) sidewalls, achieved by high-
125 precision computer-controlled motors, simulates an initial rifting phase inducing uniform orthogonal
[extension-divergence](#) into the overlying brittle and viscous model materials that represent the brittle upper
crust and ductile lower crust, respectively. For orthogonal convergence during the subsequent inversion
phase, the sidewalls are simply moved together again. During oblique divergence and oblique convergence,
[which we apply to account for possible different deformation kinematics during basin formation and
inversion, such as proposed by e.g. Marques et al. \(2014\) and Rosa et al. \(2022\)](#), additional lateral motion
130 of [the one](#) mobile base plate [on one side of the experiment](#) was applied (Fig. 2c).

In order to localize deformation in our models, creating a graben during the initial rifting phase, we
introduce a linear seed on the top of the viscous layer that was made from the same viscous material as used
for the lower crustal layer ([e.g.e.g.](#) Le Calvez & Vendeville 2002; Molnar et al., 2019, 2020; Zwaan and
Schreurs, 2017). This seed was a semi-cylindrical ridge with a c. 1 cm diameter, and was placed in the same
135 position in each model (i.e. along the central axis of the model, Fig. 2a,b).

[Our general model set-up has been regularly used for orthogonal and oblique rifting, and transpression
models \(Schreurs and Colletta, 1998, 2002; Zwaan and Schreurs, 2017; Zwaan et al., 2016, 2018a, 2020;
Schmid et al., 2022a, b\), but so far only Guillaume et al. \(2022\) have applied a similar foam-based set-up
for basin inversion modelling, with the fundamental difference that shortening in their models was
140 perpendicular to the divergence direction. Our model set-up design is also fundamentally different from
previous basin inversion model set-ups involving base plates and/or sidewalls for orthogonal and oblique
basin inversion \(e.g. Brun and Nalpas, 1996; Nalpas et al., 1995, see also Zwaan et al. 2022b, and references
therein\).](#)

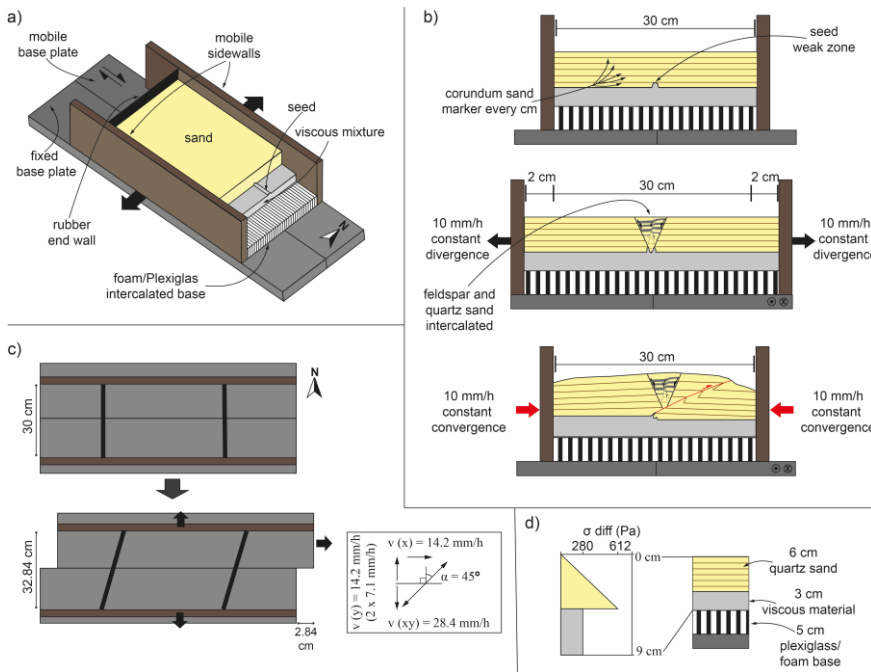
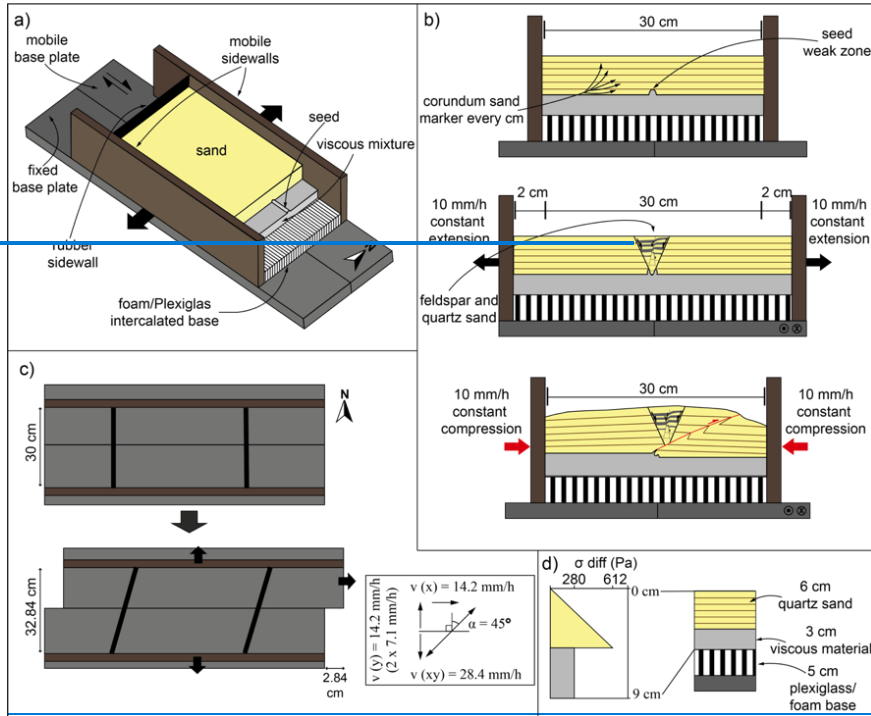


Figure 2: Experimental set-up adopted for this study. a) 3D cut-out view showing the brittle-viscous layers on top of the Plexiglas/foam base of the experiment (north arrow added for reference in the models). b) Schematic example of a sedimentation model run in 2D. c) Top view example of movement direction of the experimental apparatus used in this study (oblique ~~extension-divergence~~ example, with definition of divergence and ~~compression-convergence~~ obliquity as angle α . Note that angle α is positive for dextral oblique divergence, as well as for sinistral oblique convergence. Vice versa, angle α is negative for sinistral oblique divergence and for dextral oblique convergence.) d) Schematic strength profile indicating the crustal setting represented in our models.

150

155 2.2 Materials

We utilized brittle and viscous analogue materials (material properties summarized in Table 1) to reproduce the brittle and ductile parts of the upper and lower crust in our experiments.

A 3 cm thick viscous layer served to replicate a 10 km thick lower crust. This material consists of a near-Newtonian ($\eta = \text{ca. } 1.5 \cdot 10^5 \text{ Pa} \cdot \text{s}$; $n = 1.05\text{-}1.10$, Zwaan et al., 2018c) mixture of SGM-36 Polydimethylsiloxane (PDMS) and corundum sand ($\rho_{\text{specific}} = 3950 \text{ kg/m}^3$, <https://www.carloag.ch>). We

160

mixed the components according to a 0.965: 1.00 weight ratio, resulting in a viscous mixture with a density of ca. 1600 kg/m^3 .

We applied a 6 cm thick layer of fine quartz sand ($\phi = 60\text{-}250 \mu\text{m}$, and $\phi = 31.4\text{-}36.1^\circ$, ~~Table 4~~Zwaan et al. 2018a) sieved on top of the viscous layer, representing a 20 km brittle upper crust (~~Zwaan et al. 2018a~~).

165

The sand was flattened at 1 cm intervals with a scraper to avoid lateral variation in sand layer thickness during the model preparation. We sieved the sand from ca. 30 cm height to ensure a constant brittle layer density of ca. 1560 kg/m^3 (e.g. Klinkmüller et al., 2016; Schmid et al., 2020).

We used layers of feldspar sand (~~grain size range~~ $\phi = 100\text{-}250 \mu\text{m}$ and $\phi = 29.9\text{-}35^\circ$, Zwaan et al., 2022c) intercalated with layers of quartz sand for sedimentary infill in order to provide a visual record of syn-rift units on ~~cross~~sections (Fig. 2b). The sand application was done by hand, using a paper cone with an opening of 3 mm at the tip. The flux of sand was controlled by pressing the opening of the cone and we filled the graben up to the general model surface. ~~The use of feldspar sand as syn-rift sediment is not considered to significantly impact model evolution due to the very similar characteristics to our quartz sand (Zwaan et al., 2022).~~

170

Furthermore, we added thin $<1 \text{ mm}$ thick marker intervals of fine corundum sand (~~grain size range~~ $\phi = 88\text{-}125 \mu\text{m}$) to the quartz sand layer, which allowed for the tracing of deformation in ~~cross~~section ~~view~~ (Fig. 2b). These thin intervals were sieved in during the scraping intervals (every cm) and are not considered to have an impact on model evolution.

175

180 **Table 1: Materials properties**

Granular materials	Quartz sand ^a	Corundum sand ^b	Feldspar sand ^b
Grain size range (ϕ)	60-250 μm	88-125 μm	100-250 μm
Specific density (ρ_{specific}) ^c	2650 kg/m^3	3950 kg/m^3	ca. 2700 kg/m^3

Formatted: Font: 8 pt

Formatted Table

Formatted: Font: 8 pt

Formatted: Font: 8 pt, German (Switzerland)

Formatted: Font: 8 pt

Formatted: Font: 8 pt, German (Switzerland)

Sieved density (ρ_{sieved})	1560 kg/m ³	1890 kg/m ³	ca. 1300 kg/m ³
Angle of internal peak friction (ϕ_{peak})	36.1°	37°	35°
Coefficient of internal peak friction (μ_{peak}) ^d	0.73	0.75	0.70
Angle of dynamic-stable friction (ϕ_{dyn})	31.4°	32.0°	29.9°
Coefficient of dynamic-stable friction (μ_{dyn}) ^d	0.66	0.62	0.58
Angle of reactivation friction (ϕ_{react})	33.5°	-	32.0°
Coefficient of reactivation friction (μ_{react})	0.66	-	0.62
Cohesion (C)	9 ± 98 Pa	39 ± 10 Pa	51 Pa
▲ Viscous material	Pure PDMS^{a,e}	PDMS/corundum sand mixture^a	
▲ Weight ratio PDMS : corundum sand	-	0.965 kg : 1.00 kg	
Density (ρ)	965 kg/m ³	ca. 1600 kg/m ³	
Viscosity (η)	ca. $2.8 \cdot 10^4$ Pa.s	ca. $1.5 \cdot 10^5$ Pa.s ^f	
Type ^g	Newtonian ($n = \text{ca. } 1$) ^g	near-Newtonian ($n = 1.05\text{-}1.10$) ^g	
^a Quartz sand, PDMS and viscous mixture characteristics after Zwaan et al. (2016; 2018a, 2018b) ^b Corundum sand characteristics after Panien et al. (2006) ^c Specific densities after Carlo AG (2022) ^d $\mu = \tan(\phi)$ ^e Pure PDMS rheology details after Rudolf et al. (2016) ^f Viscosity value holds for model strain rates $< 10^{-4} \text{ s}^{-1}$ ^g Power-law exponent n (dimensionless) represents sensitivity to strain rate ^h Feldspar sand characteristics after Zwaan et al. (2022)			

Formatted: Font: 8 pt

Formatted: Font: 8 pt

Formatted: Font: 8 pt

Formatted: Font: 8 pt

Formatted: Font: 8 pt, Highlight

Formatted: Font: 8 pt, Highlight

Formatted: Font: 8 pt

2.3 Model parameters

185 For this study we completed two main series of four experiments each, and an initial series of reference
 experiments (Table 2). Series A contains our reference experiments that simulated the initial (orthogonal)
 rifting phase only, with and without syn-rift sedimentation. Series B explores the effects of basin inversion
 without syn-rift sedimentation. Series C tests the effects of syn-rift sedimentation during graben-basin
 inversion. The initial rifting phase of our Series B and C basin inversion models involved either orthogonal
 or 45° oblique divergence (where obliquity is defined by angle alpha, i.e. the angle between the normal to
 190 the rift axis and the divergence direction, Fig. 2c). The subsequent phase of shortening involved either
 orthogonal or (-)45° oblique convergence (see details in Table 2). The experiments ran for 2 hours with 40
 mm of divergence (at 20 mm/h) and another 2 hours with 40 mm of convergence, except for Models B3 and
 C3 since the initial oblique opening did not generate sufficient space for a subsequent 40 mm-of
 orthogonal divergence-convergence component of 40 mm. Therefore, total convergence in models B3 and
 195 C3 was 28 mm (over 85 min) instead, which was however sufficient convergence to establish well-
developed inversion features.

200 We implemented syn-rift sedimentation in 5 of our experiments (in Model A2 and in Models C1-4), by
 halting the machine every 15 min (8 sedimentary intervals in total) and filling the accommodation space by
 hand (pouring) with feldspar and quartz sand in alternating intervals (Fig. 2b). The two experiments with
 oblique rifting have only 7 sedimentation intervals because after the first 15 minutes, insufficient
 accommodation space was available, requiring us to start the first sand filling after 30 minutes instead.

Table 2: Parameters of analogue models performed in this study

Model Series	Model Name	Direction and velocity of divergence/convergence				Sedimentation	Cross-Sections made
		Phase 1 (40 mm of divergence)		Phase 2 (40 mm of convergence)			
		Direction (angle α)	Velocity (v) mm/h	Direction (angle α)	Velocity (v) mm/h		
Series A Reference rifting models	A1	0°	20	-	-	No	Yes
	A2	0°	20	-	-	Yes	Yes
Series B Rifting and inversion	B1	0°	20	0°	20	No	Yes ^{***}
	B2 [§]	0°	20	45°	20	No	No
	B3 ^{§§}	45°	20	0°	20	No	No
	B4	45°	20	45°	20	No	No
Series C Rifting and inversion with sedimentation	C1	0°	20	0°	20	Yes	Yes
	C2 [§]	0°	20	45°	20	Yes	Yes
	C3 ^{§§}	45°	20	0°	20	Yes	Yes
	C4	45°	20	45°	20	Yes	Yes

[§] Sections not used in this paper, presented in the supplementary material

- Formatted: Font: 7,5 pt
- Formatted: Left
- Formatted Table
- Formatted: Centred
- Formatted: Left
- Formatted: Font: 7,5 pt
- Formatted: Left
- Formatted: Font: 7,5 pt
- Formatted: Left
- Formatted: Font: 7,5 pt, Superscript
- Formatted: Font: 7,5 pt, Not Highlight
- Formatted: Font: 7,5 pt
- Formatted: Font: 7,5 pt
- Formatted: Font: 7,5 pt
- Formatted: Left
- Formatted: Font: 7,5 pt, Superscript
- Formatted: Font: 7,5 pt, Not Highlight
- Formatted: Font: 7,5 pt
- Formatted: Font: 7,5 pt
- Formatted: Font: 7,5 pt
- Formatted: Font: 6,5 pt

~~Models with reduced inversion time due to the oblique extension divergence with reduced orthogonal opening divergence component. Models with initial orthogonal extension divergence underwent dextral inversion ($\alpha = -45^\circ$) due to technical limitations of our model apparatus. However, one can simply mirror the result to obtain the sinistral inversion equivalent ($\alpha = 45^\circ$)~~

~~Models with reduced inversion time due to the oblique divergence with reduced orthogonal divergence component.~~

~~Sections not used in this paper, presented in the supplementary material~~

Formatted: Font: 7,5 pt

205

2.4 Scaling

Model scaling is important to guarantee that experiments completed in the laboratory are representative of their counterparts in natural examples/nature. For the brittle materials, the main parameter is the angle of internal friction (35° - 37°), which is similar to internal friction angle values found in the upper crust (31° - 38° , Byerlee, 1978, Table 3).

210

In order to scale the viscous material, we must consider its strain rate-dependent rheology. The stress ratio between model and nature (σ^* , convention: $\sigma^* = \sigma_{\text{model}} / \sigma_{\text{nature}}$) is calculated as follows: $\sigma^* = \rho^* \cdot h^* \cdot g^*$, where ρ^* , h^* and g^* represent density, length, and gravity ratios, respectively (Hubbert, 1937; Ramberg, 1981). Combined with the viscosity ratio (η^*), the stress ratio yields the strain rate ratio $\dot{\epsilon}^*$ (Weijermars and Schmelting, 1986): $\dot{\epsilon}^* = \sigma^* / \eta^*$. Subsequently, the velocity and time ratios (v^* and t^*) are derived from the strain rate ratio: $\dot{\epsilon}^* = v^* / h^* = 1 / t^*$. We adopt a relatively high lower crustal viscosity of ca. $5 \cdot 10^{21}$, representing a typical early magma-poor rift system (e.g. Buck, 1991). Thus, one hour in our model represents ca. 1.3 Myr in nature, and 20 mm/h of extension/compression rate divergence/convergence in the model embodies a realistic deformation velocity of ca. 5 mm/yr in nature. The scaling parameters are presented in Table 3.

220

The dynamic similarity of the model and natural example can also be examined. Firstly, the dynamic similarity between the model brittle layer and its upper crustal equivalent can be determined through the ratio R_s between the gravitational stress and the cohesive strength or cohesion C (Ramberg, 1981; Mulugeta, 1988): $R_s = \text{gravitational stress/cohesive strength} = (\rho \cdot g \cdot h) / C$. The 9 Pa cohesion in the sand and a natural cohesion of 5 MPa for upper crustal rocks, gives us a R_s of 102 and 110 for model and nature, respectively. Secondly, the dynamic similarity between our viscous material and lower crust equivalent is derived from the Ramberg number R_m (Weijermars and Schmelting, 1986): $R_m = \text{gravitational stress/viscous strength} = (\rho \cdot g \cdot h^2) / (\eta \cdot v)$, and both have the value of 68. We consider our models properly scaled since their R_s and R_m values are the same similar as to their natural equivalent.

225

230

Formatted: Space After: 0 pt, Don't adjust space between Latin and Asian text, Don't adjust space between Asian text and numbers

Formatted: Subscript

Formatted: Subscript

Formatted: Subscript

Formatted: Subscript

Formatted: Subscript

|

235 Table 3: Scaling parameters

		Model	Nature
General parameters	Gravitational acceleration (g)	9.81 m/s ²	9.81 m/s ²
	Divergence velocity (v)	5.6 · 10 ⁻⁶ m/s	1.7 · 10 ⁻¹⁰ m/s
Brittle layer	Material	Quartz sand	Upper crust
	Peak internal friction angle	35°-37°	31-38°
	Thickness (h)	6 · 10 ⁻² m	2 · 10 ⁴ m
	Density	1560 kg/m ³	2800 kg/m ³
	Cohesion (C)	9 Pa	5 · 10 ⁶ Pa
Viscous/ductile layer	Material	PDMS/corundum sand mixture	Lower crust
	Thickness (h)	3 · 10 ⁻² m	1 · 10 ⁴ m
	Density	1600 kg/m ³	2900 kg/m ³
	Viscosity	1.5 · 10 ⁵ Pas	1 · 10 ²¹ Pas
Dynamic scaling values	Brittle stress ratio (R _s)	102	110
	Ramberg number (R _m)	68	68

Formatted: Font: 9 pt

Formatted: Font: 9 pt

Formatted: Font: 9 pt

Formatted: Font: 9 pt

Formatted: Font: 9 pt

2.5 Model monitoring and analysis

240 The experiments were primarily monitored through time-lapse photographs of the model surface, taken every minute for the duration of the model run. One central camera (Nikon D810, 36 MPx) provided map view pictures, while two obliquely oriented cameras (D810, 36 MPx) were positioned on both sides of the central one to provide stereoscopic imagery. The central camera was controlled using ~~the~~ Nikon Camera Control Pro software and cameras for stereoscopic imagery were remotely triggered by passing on the signal from the central camera via an ESPER Triggerbox (Schmid et al., 2022).

245 To facilitate the first order ~~of~~ surface deformation analysis, we sieved a thin grid (4 by 4 cm) of corundum sand on the model surface. We furthermore sprinkled the model surface with coffee powder to provide markers for later Digital Image Correlation (DIC) analysis. For the models involving syn-rift sedimentation, a fine layer (< 1 mm) of quartz sand was sieved on the top of the experiment at the end of rifting phase to create a blank surface for a new grid and new coffee markers, allowing for optimal tracing of deformation during the inversion phase. Note that we defined a North reference in ~~the the~~ models ~~apparatus~~ in order to facilitate ~~the~~ description of ~~our model the~~ results (Fig. 2)

250 To quantify and visualize the surface deformation evolution of the experiments, we applied a detailed analysis of the time-lapse photographs through DIC techniques (e.g. Adam et al., 2005; Boutelier et al., 2019; Marshak et al., 2019; Zwaan et al., 2021; Schmid et al., 2022). The DIC analysis was performed by comparing top view images of subsequent time steps using LaVision's DaVis software (version 10.2). We used a calibration plate with a cross pattern of known dimensions as a reference to unwarp and rectify images and scale calculated displacements. Maximum and ~~Minimum~~ ~~minimum~~ normal strains are defined as the magnitude of the largest (i.e., stretching) and smallest (i.e., shortening) axes of the strain ellipse, and are independent of ~~eoordinate orientation~~ ~~reference frame~~ (e.g. Broerse et al., 2021). It is therefore a suitable marker to quantify extension and shortening (~~extensional and compressional deformation~~) in our experiments, respectively.

260 To reconstruct the model topography in detail, we used the pair of high-resolution oblique photographs for selected time steps. Agisoft Photoscan photogrammetry software served to merge this pair of synchronous photographs, using marked coordinates in the experiment for geo-referencing, and to create digital elevation models (DEMs) ~~for the end of Phase 1 and 2~~ at the end of both the rifting and inversion phases. The DEMs, shown in map view, as well as the extracted topography profiles over time, are combined with the PIV results for a complete interpretation of model surface evolution (e.g. Maestrelli et al., 2020; Zwaan et al., 2022a).

270 Finally, ~~eross~~ sections were made to reveal the internal structures of the models at the end of the model run (at the end of the rifting phase for Series A models, and after inversion for Series B and C). In order to produce these ~~eross~~ sections, we added water with soap at the edges of the model until the sand was saturated and stable, and cut 6 sections orthogonal to the model axis, each 10 cm apart. Pictures were taken for analysis of internal structures, and ~~the~~ quantification of subsidence. The ~~eross~~ sections of the reference models (Series A) provide insights into ~~the~~ graben structures ~~s~~ prior to inversion.

3 Results

The results of our model analysis are presented in summary figures for each experiment (Figs. 3-8). We show the incremental maximum and minimum normal strain from the DIC analysis for the early stage (first 30 minutes) and end stage of each phase (90-120 minutes interval), topography maps for the end of each deformation phase, and topographic profiles over 30 minutes increments. Model cross-sections are presented for Series A and C, and for one model in series B (Model B1).

3.1 Series A – Reference models

The Series A models provided a reference for the Series B and C analysis. These models had a constant orthogonal divergence direction ($\alpha = 0^\circ$) and a divergence velocity of 20 mm/h (Fig. 3). In Model A1 no sedimentation occurred during rifting, whereas in Model A2, eight phases of syn-rift sedimentation were applied at 15 minutes intervals.

3.1.1 Orthogonal rift without syn-rift sedimentation - Model A1

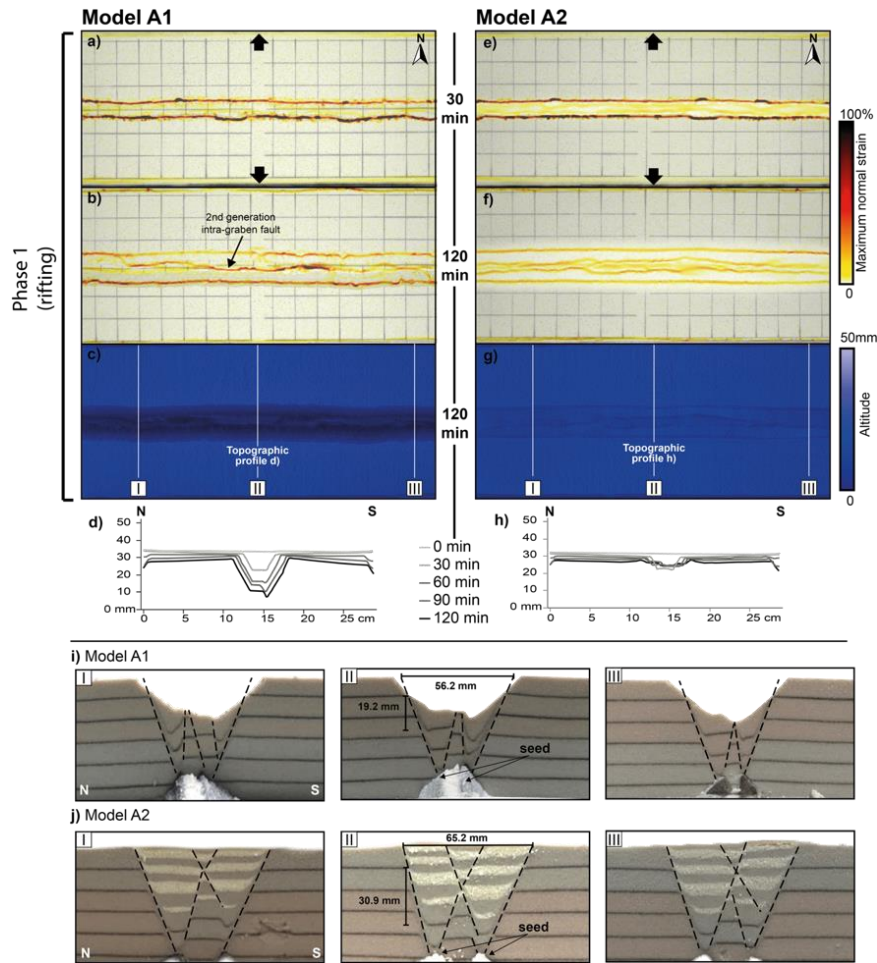
Deformation in Model A1 became highly localized in the first 30 minutes of the Model A1 run (Fig. 3a), forming with two graben-boundary faults rooting in the viscous seed (Fig. 3i_{III}); which accommodated/ accommodating extension in one E-W striking graben. Towards the end of the rifting phase ($t = 120$ min, Fig. 3b), a second-generation intra-graben fault developed between the two conjugate graben boundary faults. The strain analysis indicates higher strain values in the southern graben border fault and within the second-generation intra-graben fault (Fig. 3b). However, the northern graben border fault also remained active until the end of the experiment (Fig. 3b). Cross-section view shows drag folds related to associated with the northern and southern graben boundary faults (Fig. 3i). The final topography profiles (Fig. 3d; $t = 60$ min, 90 min and 120 min) show a v-shaped depression in topography on the southern side of the graben floor. This topographic feature can be related to the drag fold of the southern graben block seen in cross-section view (Fig. 3i_{II}), indicating that the drag fold initiated after the first hour of experiment and continued evolving until the end of the rifting phase. In the middle cross-section II (Fig. 3i_{II}), we measured graben width between the two master faults bounding the grabens border faults and the value is 56.2 mm. To measure the total fault offset, we used the uppermost corundum sand marker that showed a total of 19.2 cm of vertical downward displacement/subsidence of 19.2 mm in total.

3.1.2 Orthogonal rifting with syn-rift sedimentation – Model A2

At the early rifting stages of Model A2 ($t = 30$ min), strain analysis shows the concentration of deformation concentrating at the graben boundary faults (Fig. 3e). However, during these early rifting stages, the maximum normal strain values are lower inside the graben (Fig. 3e,f) than observed in Model A1 (Fig. 3a,b). Later in the Towards the end of the model run experiment, strain was homogeneously distributed between the boundary faults and the set of conjugate faults in the middle-center of the graben (Fig. 3f,j). The syn-rift sedimentation in Model A2 (Fig. 3j) caused an increase of graben width and

315

subsidence compared to the rifting phase without sedimentation in Model A1 (Fig. 3i): the offset of the first corundum sand marker shows a difference of \sim ca. 1 cm between Model models A1 (19.2 mm; Fig. 3ii) and A2 (30.9 mm; Fig. 3jii), and the graben structure was \sim ca. 1 cm wider in Model A2 (65.2 mm) than in Model A1 (56.2 mm).



320

325

Figure 3: Evolution of deformation during rifting for Model A1 and A2. a) and b) e) and f) displays top view maximum normal strain results for early and late-stage rifting, respectively. c) and g) show top views of digital elevation models at the end of rifting. d) and h) Topographic profiles for every 30 minutes of rifting. e) and f) display top view model DIC analysis for Maximum normal strain at early and late rifting stage. g) Digital elevation model for late rifting stage. h) Topographic profiles for every 30 minutes of rifting. Note that topography is shown prior to syn-rift sedimentation for that interval. i-j) Cross-sections for Model A1 and Model A2, respectively. Section locations are indicated in (b) and (f). Graben geometry measurements are indicated in the middle cross-sections (ii and jii).

- Formatted: Subscript
- Formatted: Subscript
- Formatted: Font: (Default) +Body (Calibri), Not Bold, Italic
- Formatted: Normal, Left

330

3.2 Series B – inversion without sedimentation

335

Here we show the results for the ~~series~~ Series B models that underwent two deformation phases (rifting and inversion) but without syn-rift sedimentation. We first present ~~M~~models B1 and B2 that involved orthogonal rifting, followed by ~~M~~models B3 and B4 with oblique rifting. These model pairs ~~subsequently between then~~ underwent either orthogonal or oblique inversion.

340

3.2.1 Orthogonal rifting –~~followed by orthogonal (Model B1) and or oblique (Model B2) inversion (B2)~~

345

The results from ~~M~~models B1 and B2 show very similar outcomes ~~between them after~~ at the end of phase 1 and are also very similar to reference Model A1 (Figs. 3a-b; 4a-b and i-j). Early rifting (~~t = 30 min~~, Fig. 4a and i) localized more strain along the graben normal faults than in the later rift phase ~~as~~; during the late rift stage (~~t = 120 min~~, Fig. 4b and j), strain was distributed between the graben boundary faults and the intra-graben faults. ~~The~~Topography analysis (Fig. 4c, g, k and o) shows a ~~maximum~~ graben subsidence of ~~~ca. 20 mm in both models~~.

350

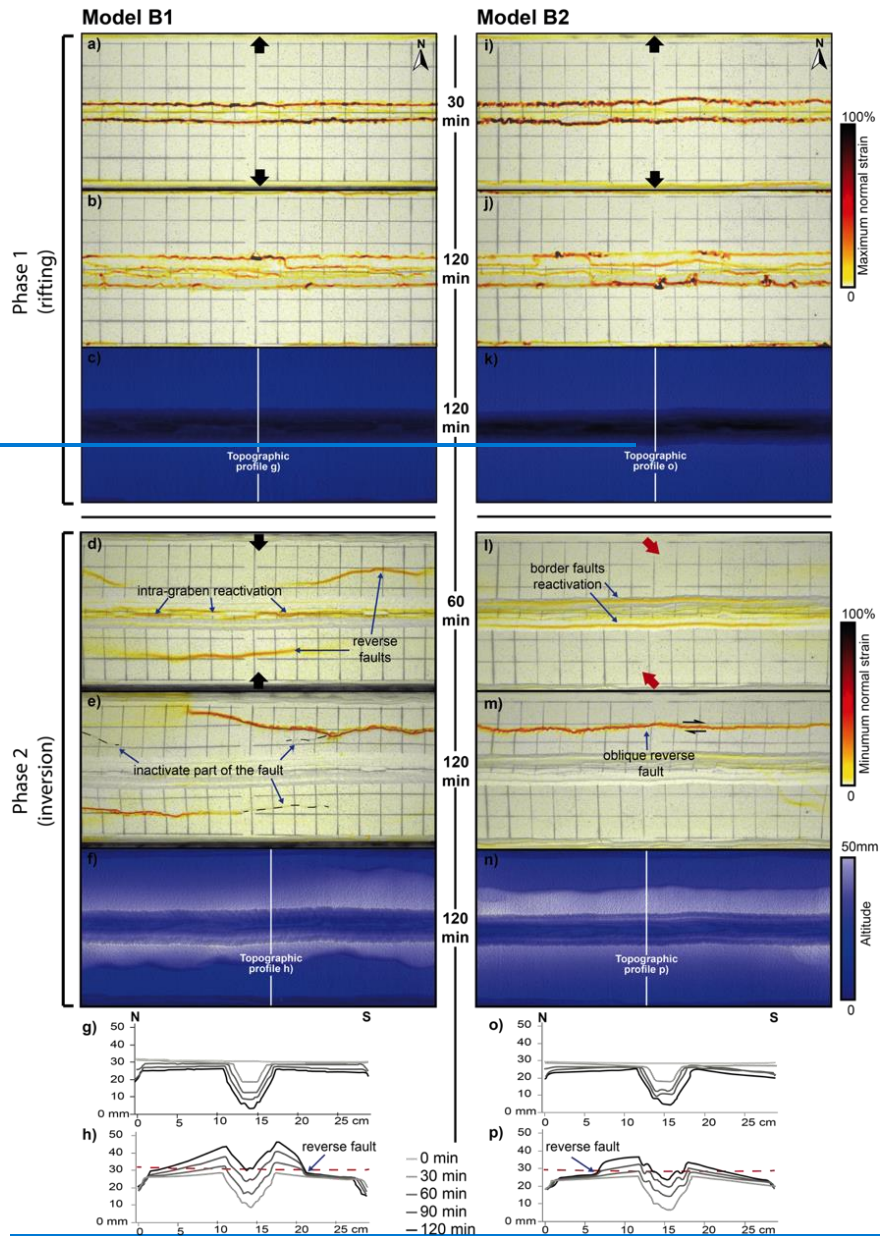
~~During~~After the ~~first 60 minutes of~~ orthogonal inversion ~~phase~~, Model B1 ~~initially first 60 minutes~~ localized strain both along the intra-graben faults and along new reverse faults on both sides of the graben (Fig. 4d). Towards the end of the model run, most parts of the southern reverse fault became relatively inactive while the northern reverse fault grew and localized higher strain (Fig. 4e). ~~At~~During the ~~final~~~~this~~ stage (~~t = 120 minute~~), also the intra-graben faults had become inactive (Fig. 4e). The areas immediately adjacent ~~to the~~ north and south ~~to~~ of the graben were uplifted, while the ~~bottom floor~~ of the inverted graben reached the same elevation as the pre-rift surface (Fig. 4f, h).

355

After the first ~~60 minutes hour~~ of oblique inversion in Model B2, strain was localized along the graben ~~border boundary~~ faults (Fig. 4l) showing direct reactivation of the original graben faults only, in clear contrast to the orthogonal inversion of Model B1 (Fig. 4d). At the end of ~~Phase 2~~, however, a single oblique reverse fault had appeared at the model surface grid, north of the graben, while all previous rift related faults were inactive (Fig. 4m). The final topography ~~data shows~~ a significantly higher maximum elevation than the pre-rift surface of ~~~ca. 15 mm~~ in orthogonal inversion Model B1 (Fig. 4f, h), while the oblique inversion Model B2 (Fig. 4n, p) had ~~an~~ ~~~ca. 7 mm~~ higher elevation than the pre-rift surface.

360

Formatted: Highlight



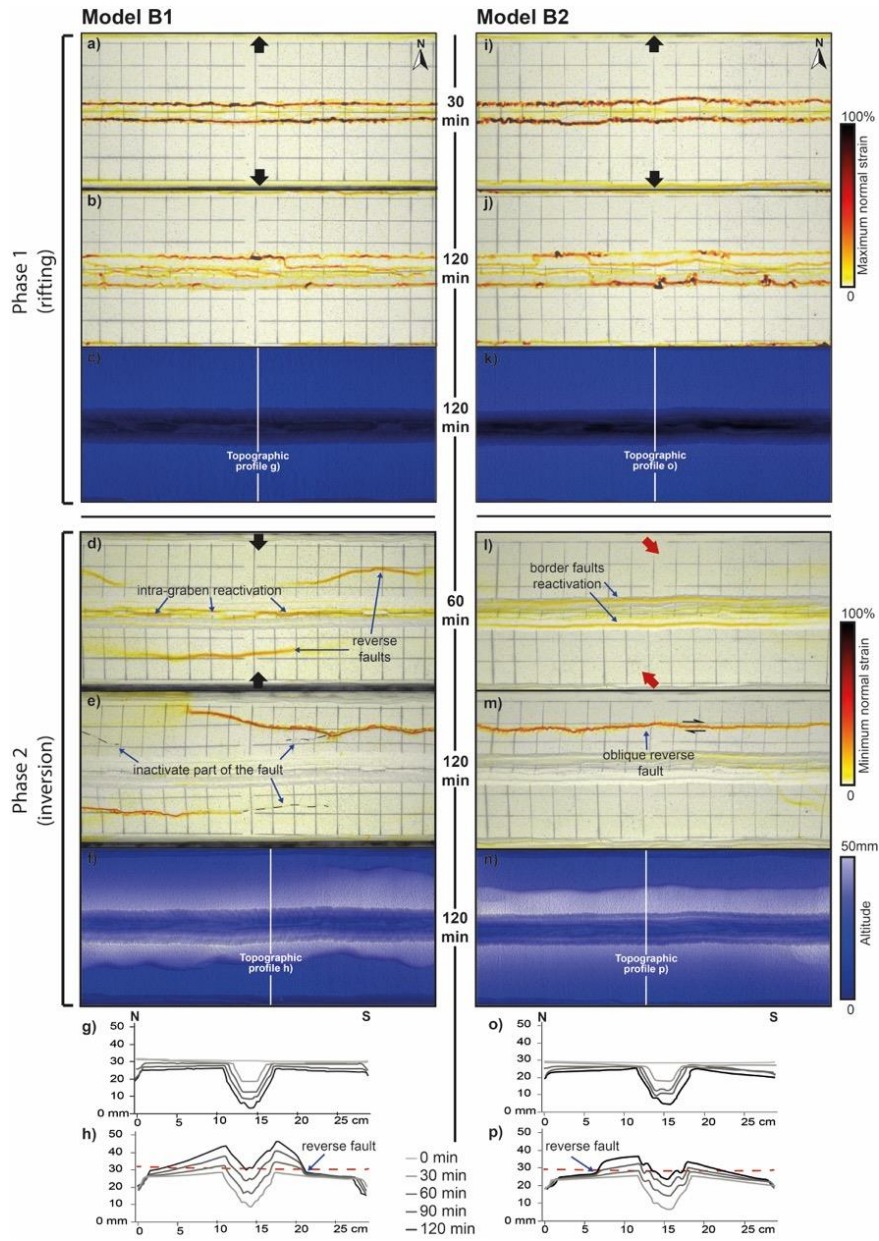


Figure 4: Evolution of deformation during rifting and inversion for models B1 and B2. a, b) and i-j) Top view maximum normal strain results for early and late-stage rifting, respectively. c, k) Digital elevation models at the end of rifting. d, e) and l, m) Top view minimum normal strain results for early and late-stage inversion, respectively. f, n) Top view of digital elevation model at the end of inversion. g, o) Topographic profiles for every 30 minutes of rifting. h, p) Topographic profiles for every 30 minutes of inversion. a) and b) displays Top view model DIC analysis for maximum normal strain at early and late rifting stages. c) and k) Digital elevation models for late rifting stage. d, e) and l) and m) displays Top view model DIC analysis for minimum normal

370 ~~strain. f) and n) Digital elevation models for late inversion stage. g, o) Topographic profiles for every 30 minutes of rifting phase. h, p) Topographic profiles for every 30 minutes of inversion phase. The dashed red horizontal line indicates the initial surface level at the start of the model run.~~

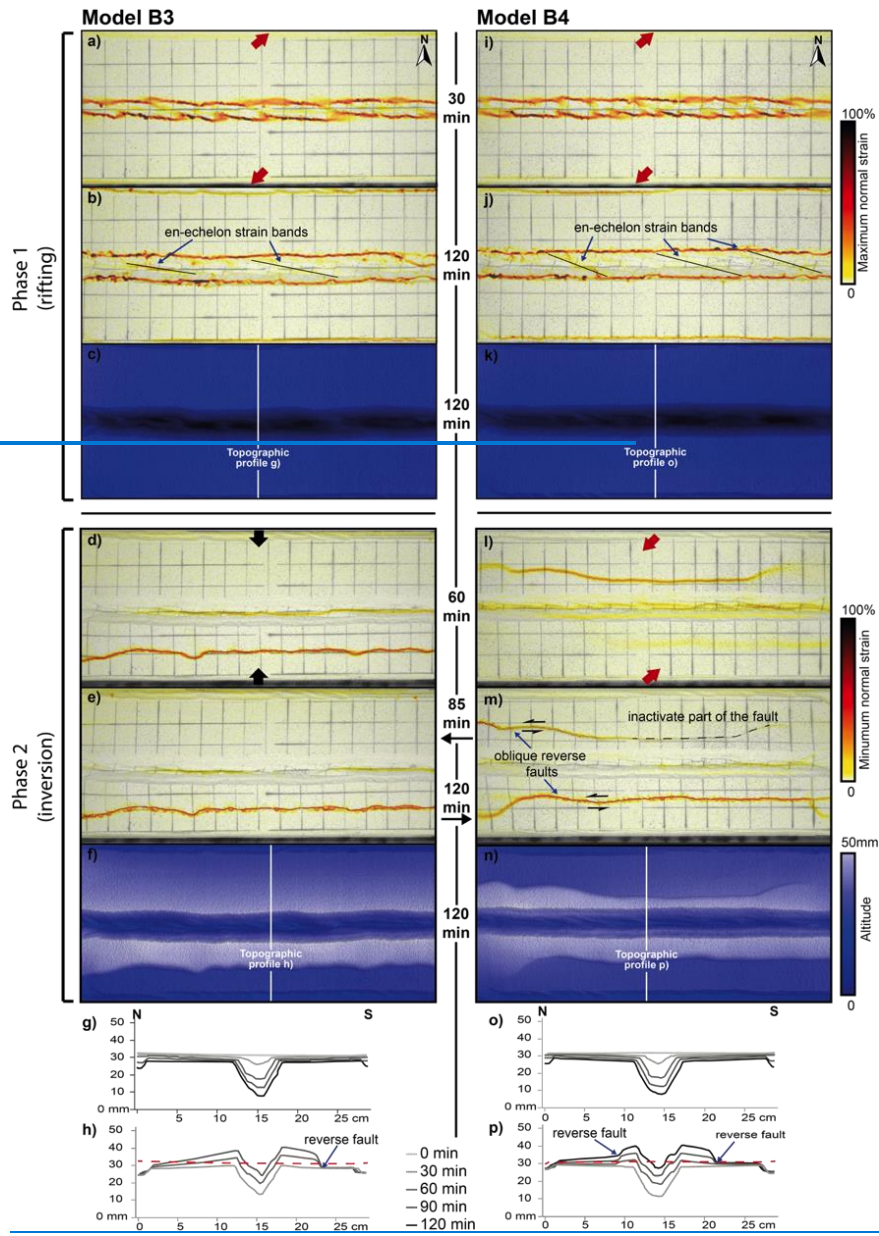
3.2.2 Oblique rifting ~~–followed by orthogonal (Model B3) and/or oblique (Model B4) inversion (B4)~~

375 ~~Oblique rifting ($\alpha = 45^\circ$) of Mmodels B3 (Fig. 5a) and B4 (Fig. 5i), with 45° oblique rifting, resulted in the development of two bands of ~~en-echelonen~~ *échelon* normal faults bounding an E-W striking graben after the first 30 minutes of deformation (Fig 5a,i). At the end of Phase 1, the strain results shows that these ~~en-echelonen~~ *échelon* faults had become interconnected, forming through-going, E-W striking graben-bounding normal faults, connected by oblique, WNW-ESE trending, lower strain diagonal-zones within the graben (Fig. 5b,j).~~

Formatted: Font: Symbol

380 ~~After 60 minutes, The of orthogonal inversion, of Model B3 resulted in the activation showed the formation of a new straight fault along the central axis of the graben and the formation-development of a new reverse fault south of the graben (Fig. 5d,e). By the end of the inversion phase, after 120 minutes, the reverse fault remained active while the fault in the middle-of-centre of the graben started-became less active, with some parts being completely inactive (Fig. 5e). Uplift was more prominent in the area between the reverse fault and the graben, while-whereas in the northern part of the experiment-model a more widespread uplift is-was recorded (Fig. 5f, g).~~

390 ~~After the first hour-60 minutes of oblique inversion in Model B4, the diagonal-goblique low strain zones within the graben structures were partially reactivated, while a significant portion of the deformation localized in a new reverse fault to the north of the graben, and deformation started to localize in the southern area of the experiment-model as well (Fig. 5l). During the later stages-After 120 minutes of inversion, the northern reverse fault became almost completely inactive, and deformation localized on the southern reverse fault (Fig. 5m). The map view grid analysis showed the oblique movement of-along the reverse faults (Fig. 5m). Rift faults concentrated-experienced only minor reactivation and became almost completely inactive by the end of the inversion phase (Fig. 5m; 120 minutes). The topography profiles indicate uplift of the rift structures (17 mm elevation of the bottom-of-the-graben floor) and the new reverse faults on both sides of it (Fig 5p), and while the northern reverse fault became inactive, widespread distributed uplift affected the northern part of the model (Fig. 5p). Along the topographic profile, the maximum uplift not-related-to-away from the reverse faults was 5 mm in the north (where the fault became inactive) and 2 mm in the south.~~



Formatted: Don't keep with next

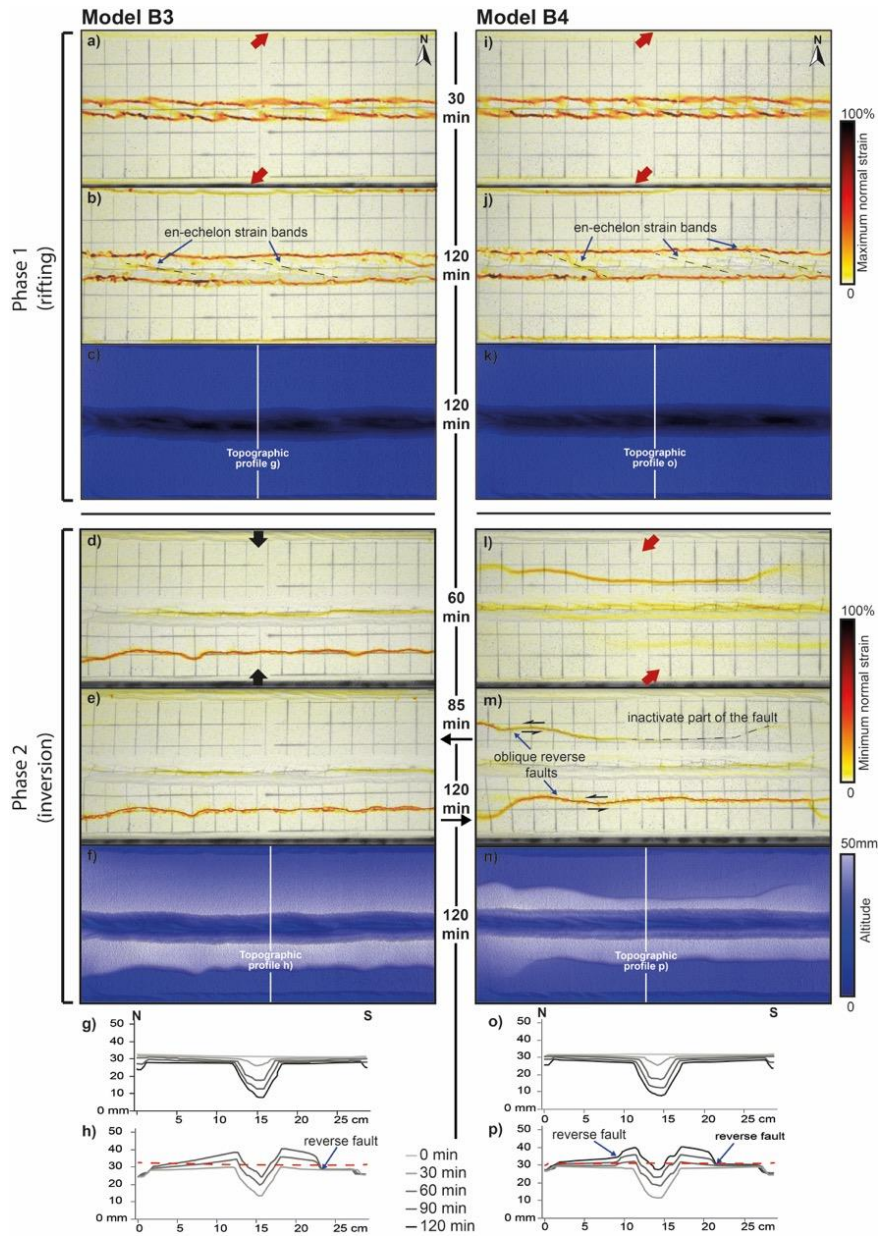


Figure 5: Evolution of deformation during rifting and inversion for **Models B3 and B4**. **Top view maximum normal strain results for early and late-stage rifting, respectively. c, k) Digital elevation models at the end of rifting. d, e) and l, m) Top view minimum normal strain results for early and late-stage inversion, respectively. f, n) Top view of digital elevation model at the end of inversion. g, o) Topographic profiles for every 30 minutes of rifting. h, p) Topographic profiles for every 30 minutes of inversion. The dashed red horizontal line indicates the initial surface level at the start of the model run. Note that a, i, and b, j) display (Top view model DIC analysis for Maximum normal strain at early and late rifting stage, respectively. c, k) Digital elevation models for late rifting stage. d, l, and e, m) display (Top view model DIC analysis for Minimum normal strain. f and**

n) Digital elevation models for late inversion stage, g and o) Topographic profiles for every 30 minutes of rifting phase, h and p) Topographic profiles for every 30 minutes of inversion phase. Model B3 has a reduced inversion time of 85 minutes instead of 120 minutes, as indicated in the figure.

415 3.3 Series C – inversion with sedimentation

Here we present the results for our Series C models with the rifting phase divided in 8 sedimentation intervals of 15 minutes each, with 20 mm/h of displacement during both the rifting and subsequent convergence phases. The results are presented in pairs according to the models' initial divergence direction (orthogonal and oblique, $\alpha = 0^\circ$ and $\alpha = 45^\circ$, respectively) (Figs. 6, 8).

420

3.3.1 Orthogonal rifting with sedimentation – followed by orthogonal (Model C1) and/or oblique (Model C2) inversion (C2)

The early stages of rifting of both models C1 and C2 resulted in high strain localization in the graben border-boundary faults and lower strain rates inside the graben (Fig. 6a,i). During later rifting stages, the maximum normal strain values were lower along the graben border-boundary faults and instead rather evenly distributed among all faults within the graben (Fig. 6b,j). These results for the early and late stages of rifting show great similarity to the ones in results from Model A2 (Fig. 3e,f). Cross-section thickness measurements from each of the 15 minutes syn-rift sedimentation intervals (I1-I8), indicate a progressive increase of subsidence in the first two sedimentation intervals (up to 8 mm/interval, inset in Fig. 7a; I1 to I3). From interval I4 to I8, we observed a decrease in the subsidence rate (down to ca. 4 mm/interval, inset in insets in Fig. 7a; I4-8).

430

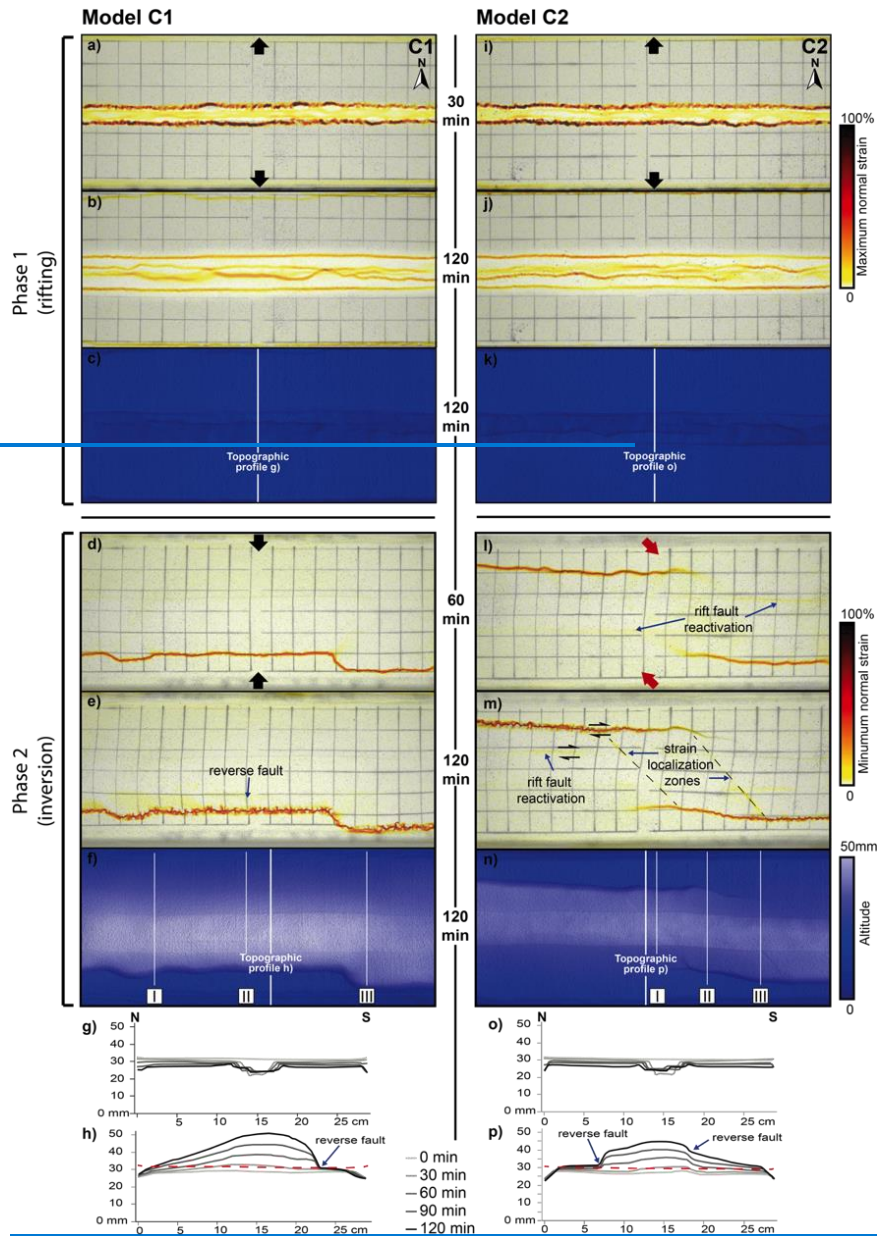
The orthogonal inversion in Model C1 (Model C1, Fig. 6d-e) concentrated deformation on a new reverse fault at the southern part of the model (Fig. 6d-e). Strain data show high localization along this reverse fault, while no reactivation at all is visible in the previous inherited rifting structures. In cross-section view (Fig. 7a_{II}) it becomes clear that the whole graben structure was uplifted by the reverse fault while the model surface was folded. The section shows that there is a curved and thick shear zone along the reverse fault, in fact a ca. 1 cm thick shear zone by the end of the model run, that was seeded in the viscous layer, the latter which itself also rose during rifting was also thickened (most probably already during rifting as seen in sections from models A1 and A2, Figs 3i, j, 7a).

435

Compared to orthogonal inversion Model C1, oblique inversion in Model C2 shows a different effect on the reactivation of previous rift structures in Model C2 (Fig. 6l-m). We observed minor reactivation of the previously formed normal-graben-bounding normal faults during the subsequent 45° oblique inversion phase, and main strain localization along newly formed reverse faults in the NW and SE quadrants, connected by strain localization zones parallel to the inversion direction. The Our topography analysis shows a small (~ca. 2 mm) pop-up structure related to minor inversion of the graben border faults (Fig. 6n,p), with a small dextral strike-slip component in-visible on the surface grid as well (Fig. 6m,n,p). In cross-section view, the newly formed reverse faults were in fact thick (ca. 1 cm) shear zones in those locations where only one of them developed, whereas the shear zones were thinner (< 5 mm) when multiple reverse faults developed (Fig. 7b).

445

|450



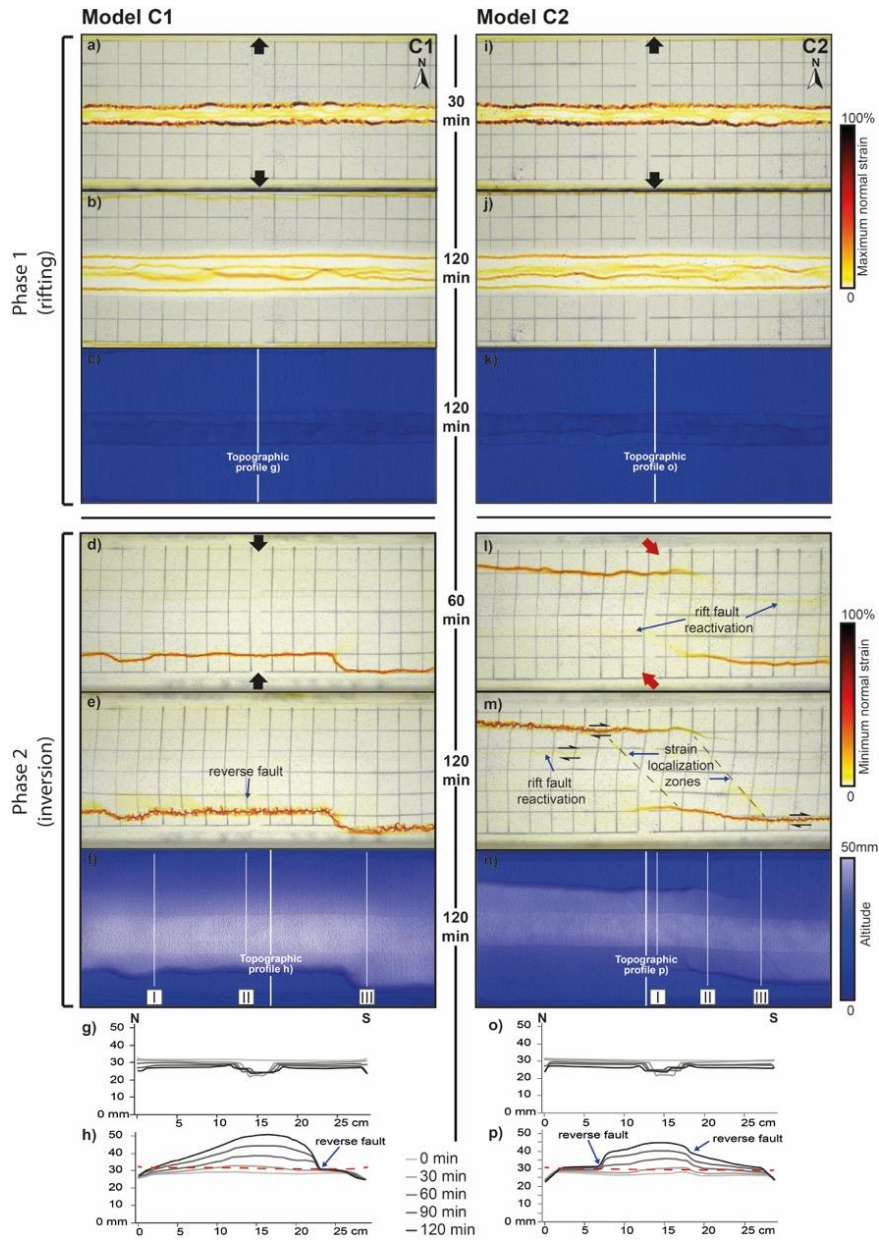
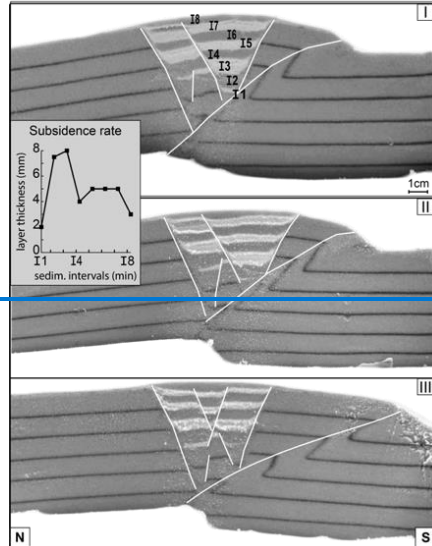


Figure 6: Evolution of deformation during rifting and inversion for ~~M4~~ models C1 and C2. a, b) and l-j) Top view maximum normal strain results for early and late-stage rifting, respectively. c, k) Digital elevation models at the end of rifting. d, e) and l, m) Top view minimum normal strain results for early and late-stage inversion, respectively. f, n) Top view of digital elevation model at the end of inversion. g, o) Topographic profiles for every 30 minutes of rifting. h, p) Topographic profiles for every 30 minutes of inversion. Topography is shown prior to syn-rift sedimentation for that interval, and the dashed red horizontal line indicates the initial surface level at the start of the model run.

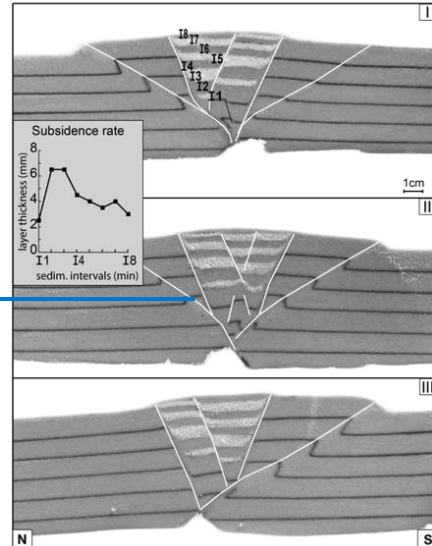
460 a), and b), i) and j) displays (Top-view model DIC analysis for Mmaximum normal strain at early and late rifting stages. c) and k) Digital elevation models for late rifting stage. d), and e), l and m) displays (Top-view model DIC analysis for Mminimum normal strain. f) and n) Digital elevation models for late inversion stage. g) and o) Topographic profiles for every 30 minutes of rifting phase. h) and p) Topographic profiles for every 30 minutes of inversion phase.

465

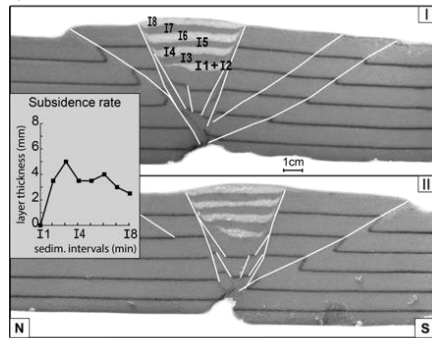
a) Model C1



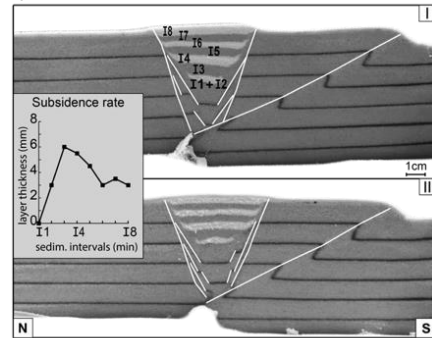
b) Model C2



c) Model C3



d) Model C4



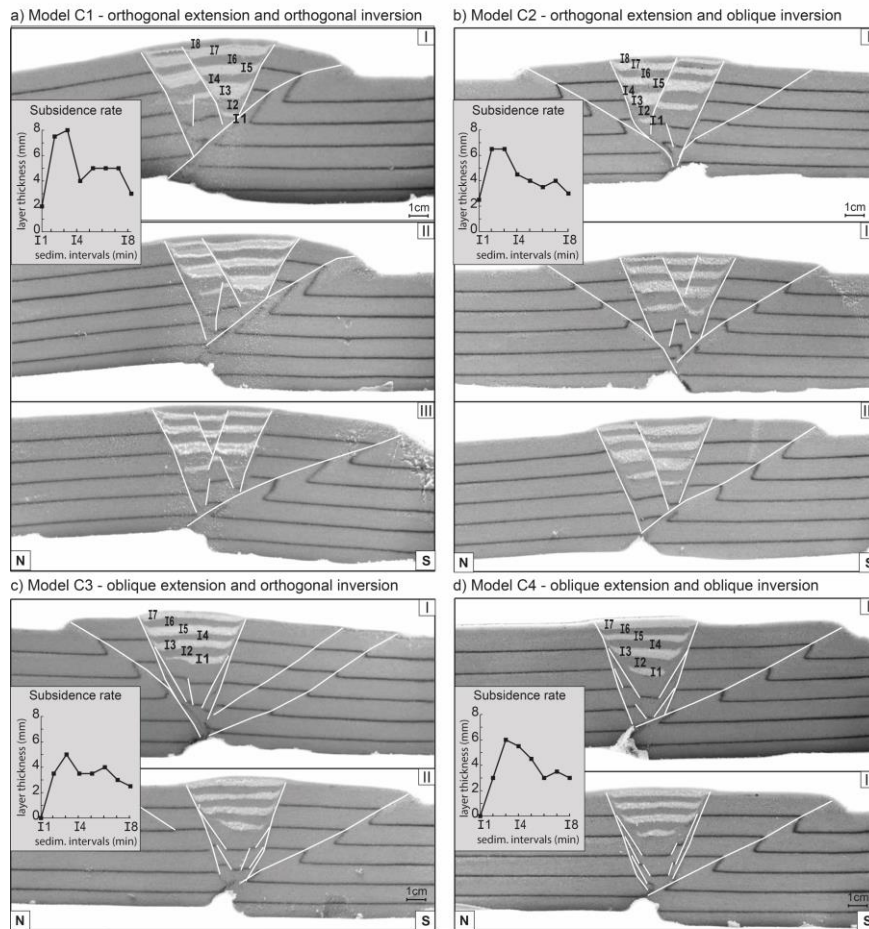


Figure 7: a), b), c) and d) Cross-sections of experiments with sedimentation and measurements on models showing the influence of extension obliquity on sedimentation and subsidence rate. a) Model C1 with orthogonal extension and orthogonal inversion phases. b) Model C2 with orthogonal extension and oblique inversion phases. c) Model C3 with oblique extension and orthogonal inversion phases. d) Model C4 with oblique extension and orthogonal inversion phases. Section locations are shown in Figs. 5 and 78. Syn-rift sedimentation units always starts with feldspar sand (white) and are divided into 8 intervals of 15 minutes of extension, except for the oblique extension-divergence models (C3 and C4), that where I1 and I2 are represented in the same unit. I1 = 15 min, I2 = 30 min, I3 = 45 min, I4 = 60 min, I5 = 75, I6 = 90 min, I7 = 105 min, I8 = 120 min (after the initiation of rifting). North (N) and South (S) references. Section orientations are indicated at the bottom section of each model.

Formatted: Not Highlight

470

475

480

3.3.2 Oblique rifting with sedimentation —followed by orthogonal (Model C3) and/or oblique (Model C4) inversion

485 Models C3 (Fig. 8a) and C4 (Fig. 8i) ~~presented developed clear en echeloned graben~~ boundary faults after the first 30 minutes of ~~experiment in response to the 45°~~ oblique rifting, thus showing ~~a similar result as results similar to M~~models B3 and B4 (Fig. 5b, i). ~~After Over the subsequent two-1.5~~ hours of rifting, the ~~en echeloned echelon~~ faults evolved into two main E-W graben boundary faults, but some faint ~~en echeloned echelon~~ strain bands remained active within the graben (Fig. 8b,j). Topography analysis shows that ~~the~~ vertical subsidence in the first 30 minutes was lower than ~~during~~ the subsequent 30 minutes
490 phases ~~(2 mm/interval vs. 4.8 mm/interval, Figs. 8g,e7c, d)~~. In fact, the first sedimentation layer (white feldspar sand in the cross-sections, Fig. 7c-d) represents 30 minutes of rifting, and the subsequent layers represents 15 minutes each, resulting in seven filling layers (Fig. 7e-d). Subsidence was indeed slower in models C3 and C4 ~~when#~~ compared to models C1 and C2: ~~it took 30 minutes of oblique rifting (two 15 minutes intervals) to create accommodation space for sedimentation, while the first 15 minutes of orthogonal rifting in models C1 and C2 created enough subsidence for applying a sedimentation interval, the first 30 minutes of orthogonal rifting subsidence is comparable with the first 15 minutes in orthogonal rifting.~~ Model C3 and C4 (Fig. 7c,d) did not develop the intra-graben normal faults seen in ~~M~~models C1 and C2 (Fig. 7a,b).

500 Orthogonal inversion in Model C3 created initial reverse faulting in the north and SE of the models, but without graben ~~normal boundary~~ fault reactivation (Fig. 8d). By the end of the experiment (Fig. 8e), after 85 minutes, the northern reverse fault became completely inactive while the southern one grew laterally (westward), remaining active. Topography analysis shows uplift limited by the reverse faults ~~lines~~ on both sides of the model (Fig. 8f,h). In ~~eross~~ section view, there is an alternation between northern (Fig. 7c) and southern (Fig. 7c₁) reverse fault activity, and we also observe that reverse faults with larger offsets had an increased thickness.

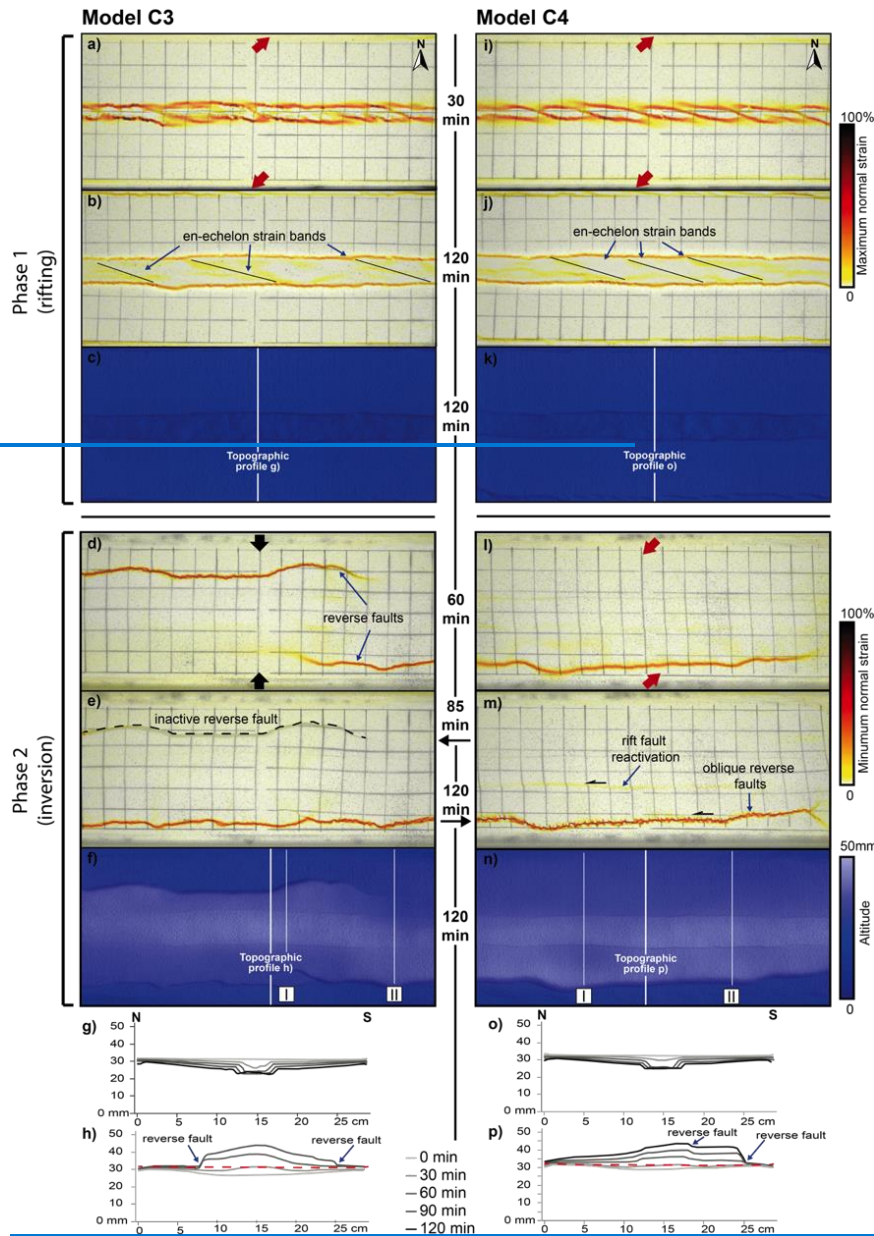
510 The oblique inversion in Model C4 (Fig. 8l-m) is predominantly accommodated by a new reverse fault in the south, with limited reactivation of the rift structures. Topography data show additional uplift in the graben in contrast to the orthogonal inversion structures in Model C3 (Fig 8f). The topographic profiles (Fig. 8p) indicate ~~a marked limited~~ inversion ~~in of~~ the graben ~~boundary faults, starting~~ after the first hour ~~and continuing~~ until the end of the experiment.

515 The ~~eross~~ sections of ~~M~~models C3 and C4 (Fig. 7c,d) revealed that the reverse fault nucleated in the seed at the base of the graben, and developed ~~into a ca. 1 cm~~ thick shear zone. Section II from ~~orthogonal inversion~~ Model C3 (Fig. 7c) shows the ~~formation presence~~ of a reverse fault north of the graben, seeding 2 cm below the surface, ~~with no clear link to the previous rift faults or to the viscous material at the base of the graben, like most of the which is in contrast to the other reverse faults shown visible in Fig. 7.~~ However, in map view (Fig. 8d-f), it is shown that this is in fact the tip of the same reverse fault present in Section I of Model C3 (Fig. 7c)

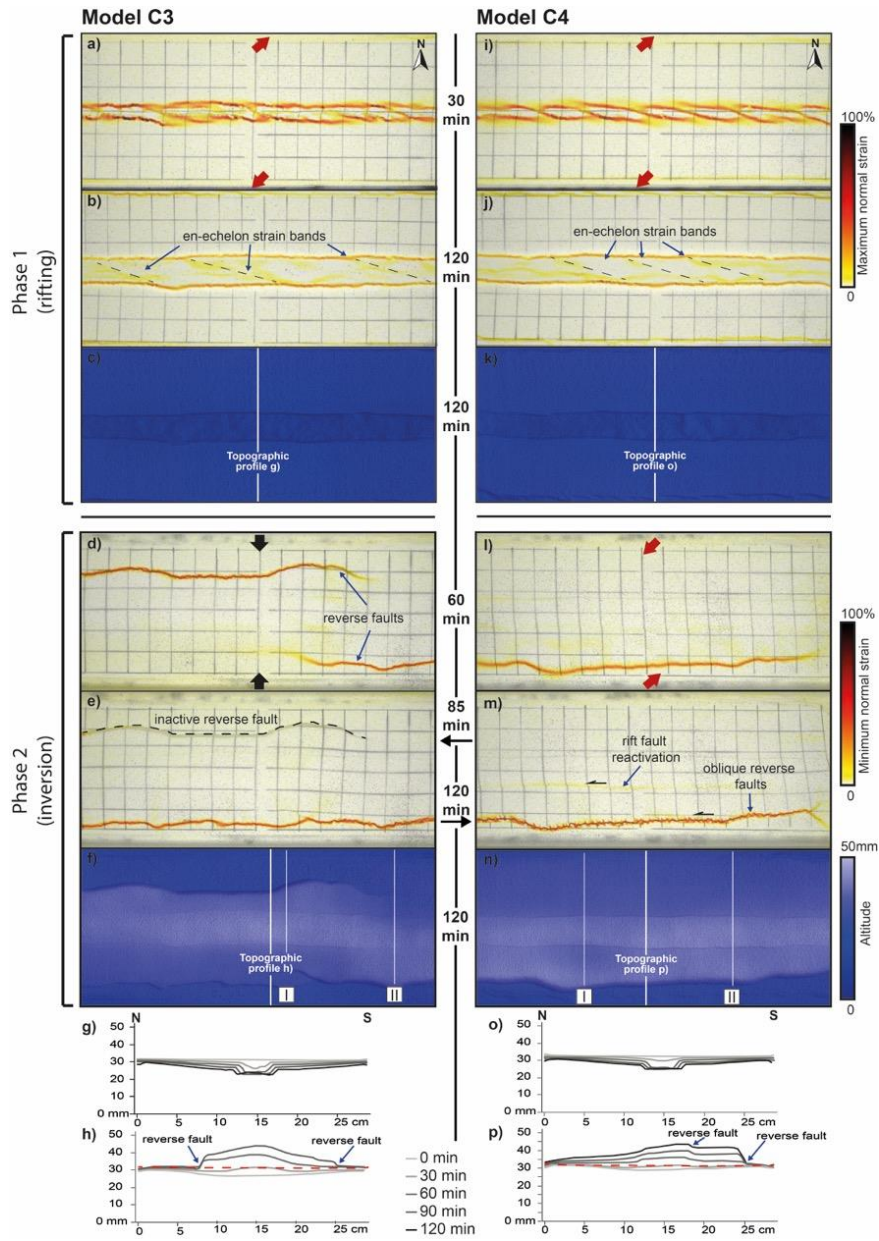
Formatted: Highlight

Formatted: Highlight

Formatted: Not Strikethrough



Formatted: Don't keep with next



520 Figure 8: Evolution of deformation during rifting and inversion for **Model C3** and **Model C4**. **a, b**) and **i-j, j**)
 525 displays **Top view model DIC analysis for Maximum normal strain results for at-early and late-stage rifting**
stage, respectively. **c, k**) Digital elevation models **for at the end of late-rifting stage**. **d, e**) and **l, m**) displays **Top**
view minimum normal strain results for early and late-stage inversion, respectively. **Top-view model DIC analysis**
for Minimum normal strain. **f, n**) **Top view of digital elevation model at the end of late inversion stage**. **g, o**)
 Topographic profiles for every 30 minutes of rifting phase. **h, p**) Topographic profiles for every 30 minutes of of
 inversion phase. Topography is shown prior to syn-rift sedimentation for that interval, and the dashed red

~~horizontal line indicates the initial surface level at the start of the model run. Note that Model C3 has a reduced inversion time of 85 minutes instead of 120 minutes, as indicated in the figure. Model C3 has a reduced inversion time as indicated in the figure.~~

530

4 Discussion

4.1 Summary and comparison to previous models

The modeling results, presented in two schematic overview figures (Figs. 9 and 10), show how ~~deformation directions imposed kinematics~~ and the presence of syn-rift sedimentation affects initial basin evolution and subsequent inversion.

535

4.1.1. Rifting phase

The overview of the rifting phase without sedimentation (Fig. 9a and b) ~~shows depicts~~ the general ~~structural differences in graben evolution structure~~ as a result of ~~different~~ divergence directions ($\alpha = 0^\circ$ and $\alpha = 45^\circ$ ~~orthogonal or oblique~~). ~~The differences in A different~~ divergence ~~orientation direction~~ resulted in different initial graben structures. However, at the final stage of rifting, the graben geometries ~~formed during orthogonal and oblique rifting~~ were very similar (Fig. 9). The main difference ~~remained occurs~~ within the graben, where ~~orthogonal divergence generated~~ parallel pairs of conjugate normal faults ~~formed due to orthogonal divergence~~, whereas oblique divergence resulted in ~~en echelon en échelon~~ structures.

540

Furthermore, oblique ~~extension divergence~~ caused a decrease in graben width compared to the orthogonal rifting models, ~~due to an increase in boundary fault dip~~, as also described in previous ~~modelling~~ studies (Tron & Brun 1991; Zwaan and Schreurs, 2016; Zwaan et al., 2018a) (Figs. 3 and 4). This reduction in width ~~and increase in fault angle~~ is caused by the strike-slip component accommodating deformation in oblique rifting settings.

545

The syn-rift sedimentation models (Fig. 10a and b) ~~demonstrated showed~~ the same initial difference in orthogonal and oblique divergence as the models without sedimentation. The oblique divergence models resulted not only in a narrower graben at the end of the extension phase, but also in a reduction of the final total subsidence observed in ~~eross~~-section (Fig. 7). A narrower graben forming during oblique rift evolution led to smaller loads of sedimentation, consequently there was less ~~weight to cause~~ graben floor subsidence.

550

However, orthogonal and oblique rifting produced a very similar subsidence evolution in response to the syn-rift sedimentation (Fig. 7). The first subsidence interval (I1) was always the smallest, while the subsequent three intervals (I2 to I4) accommodated more subsidence, and from this moment on, sedimentary intervals started ~~ed~~ thinning again until the last interval (I8). This ~~initial~~ subsidence rate ~~evolution increase likely~~ occurred because the increase in sedimentary load over time enhanced subsidence. However, the reason why we observe a subsidence decline after sedimentation interval I4 remains unclear.

555

560

Overall, concerning the total subsidence in models with and without syn-rift sedimentation, we observe that subsidence in the former case was significantly higher while the rift boundary faults remained active for a longer period of time as well. Zwaan et al. (2018a) report a similar basin evolution due to syn-rift sedimentation. In their experiments without syn-rift sedimentation, the absence of sedimentary loading

565 inside the graben leads to a smaller offset along the graben boundary faults since part of the deformation
was taken up by intra-graben faults. By contrast, in their models with syn-rift sedimentation, the graben
wedge was strengthened, so that faulting remained concentrated along the main graben boundary faults.
The latter observation was also made in numerical models by Burov and Poliakov (2001) and Olive et al.
(2014).

570

4.1.2. Inversion phase

Our experimental results have established an order of importance regarding the parameters controlling fault
575 reactivation throughout the inversion phase (Figs. 9b and 10b). It seems that the rift kinematics, i.e.
orthogonal vs. oblique rifting, have no significant influence on inversion structures as the final rift structures
were very similar. Much more important are syn-rift sedimentation and inversion kinematics.

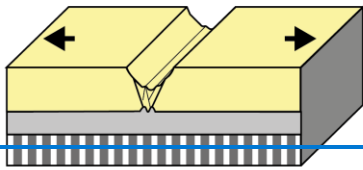
Without sedimentation, the rift structures were reactivated during inversion, and ~~the new~~ low-angle reverse
faults developed independently of inversion direction (Fig. 9). Both orthogonal and oblique inversion
580 resulted in the development of new low-angle reverse faults rooting at the base of the graben (Fig. 9). The
reactivation of the rift structures, occurred mainly at the intra graben structures in the orthogonal inversion
models (Fig. 4 and 5; ~~M~~models B1 and B3), whereas in oblique inversion models (Fig. 4 and 5; ~~M~~models
B2 and B4) both the graben boundary faults and the intra-graben faults showed significant reactivation.

The presence of syn-rift sediments (Fig. 10b) led to major differences in fault reactivation throughout the
585 inversion phase, since the basin infill acted as a buffer to reactivation of the rift structures. ~~During
orthogonal inversion graben faults did not undergo any reactivation while deformation localized in the
newly formed low-angle reverse faults (Fig. 10). In the oblique inversion models, the reactivation of
previous rift structures was observed.~~ Our models results are in accordance with previous studies that
described a similar decrease in fault reactivation when syn-rift sedimentation was applied (Pinto et al.,
590 2010b, ~~aa~~, ~~b~~; del Ventisette et al., 2006; Panini et al., 2005b; Dubois et al., 2002). By contrast, Panini et al.
(2005) found that graben infill increased rift fault reactivation. This difference was likely due to their use
of rheologically weak microbeads as graben infill, while we used feldspar and quartz sands so that the
graben infill in our models had a similar rheology to the surrounding granular materials.

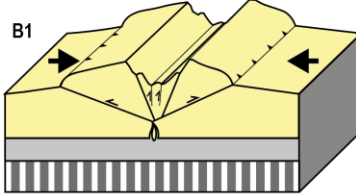
~~Furthermore, we found that during orthogonal inversion graben faults did not undergo any reactivation as
595 deformation localized in the newly formed low-angle reverse faults, whereas limited reactivation of
previous rift structures was observed in our oblique inversion models (Fig. 10). Furthermore, ~~o~~Other
studies, ~~with different analogue modelling set-ups,~~ have also shown that increasing degrees of oblique
~~compression-convergence~~ can promote normal fault reactivation (e.g., Nalpas et al., 1995; Brun and Nalpas,
1996; see also reviews by Bonini et al. 2012 and Zwaan et al. 2022b), and references therein. Indeed, while
600 analyzing inverted rift basins in nature, Ziegler et al. (1995) found that in order to facilitate normal fault
reactivation the maximum horizontal compressive stress should be at an angle $<45^\circ$ to the normal fault
strike.~~

a)

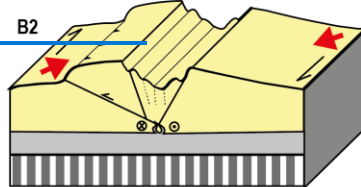
Phase 1: orthogonal extension ($\alpha = 0$)



Phase 2: orthogonal inversion ($\alpha = 0$)

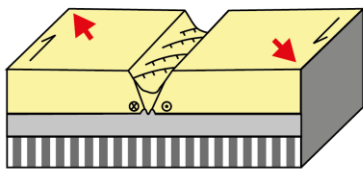


Phase 2: dextral oblique inversion ($\alpha = 45^\circ$)

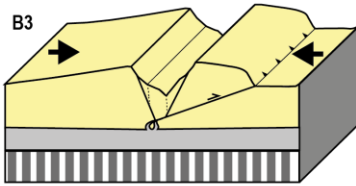


b)

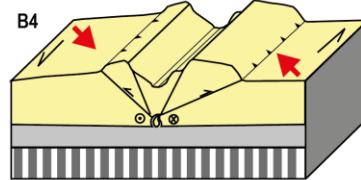
Phase 1: oblique extension ($\alpha = 45^\circ$)

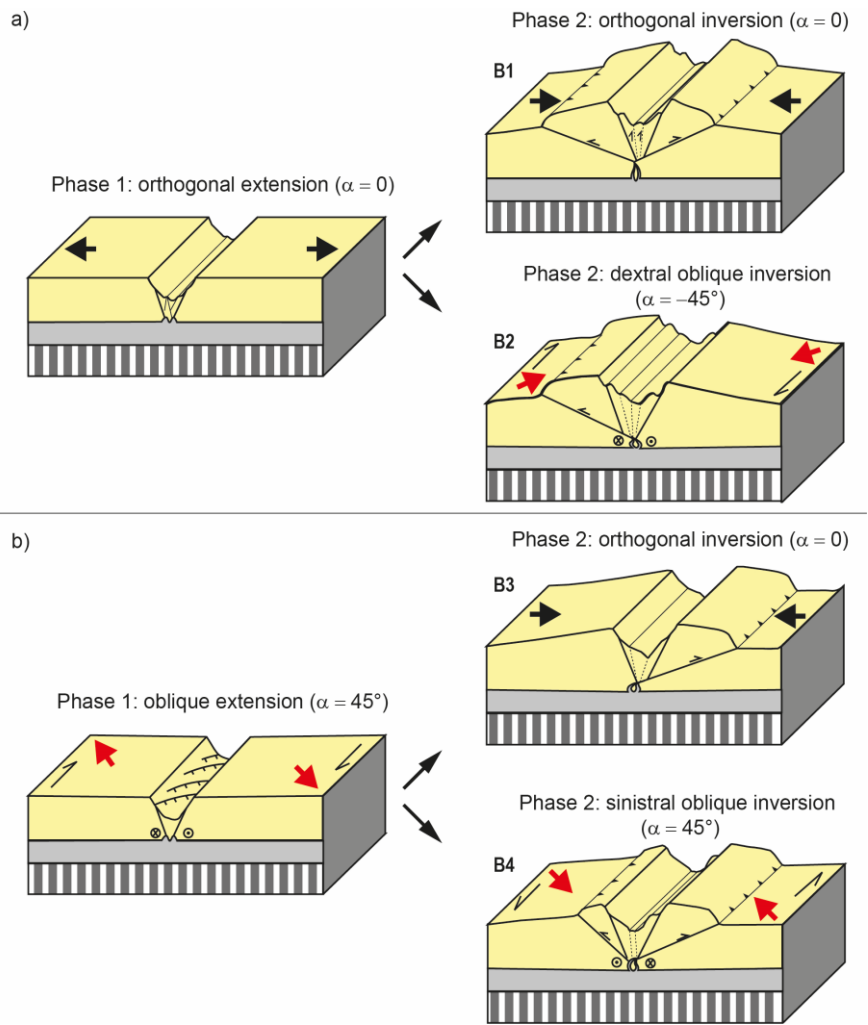


Phase 2: orthogonal inversion ($\alpha = 0$)



Phase 2: sinistral oblique inversion ($\alpha = 45^\circ$)

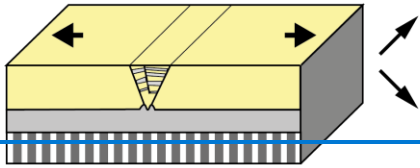




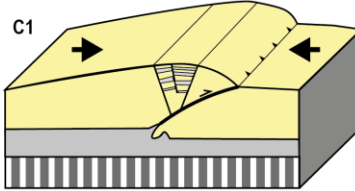
605 Figure 9: Schematic summary of our experimental results without syn-rift sedimentation

a)

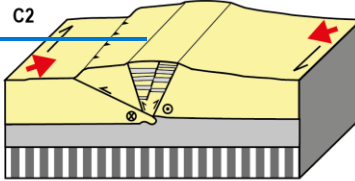
Phase 1: orthogonal extension ($\alpha = 0$)



Phase 2: orthogonal inversion ($\alpha = 0$)

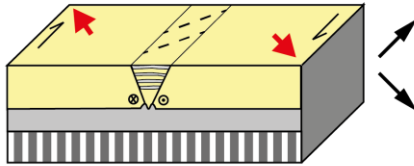


Phase 2: dextral oblique inversion ($\alpha = 45^\circ$)

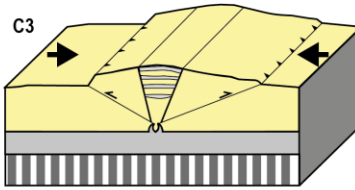


b)

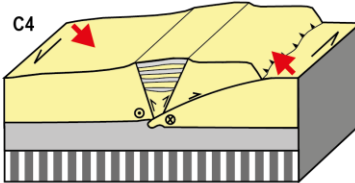
Phase 1: dextral oblique extension ($\alpha = 45^\circ$)



Phase 2: orthogonal inversion ($\alpha = 0$)



Phase 2: sinistral oblique inversion ($\alpha = 45^\circ$)



Formatted: Caption, Space After: 0 pt, Line spacing: single, Don't keep with next

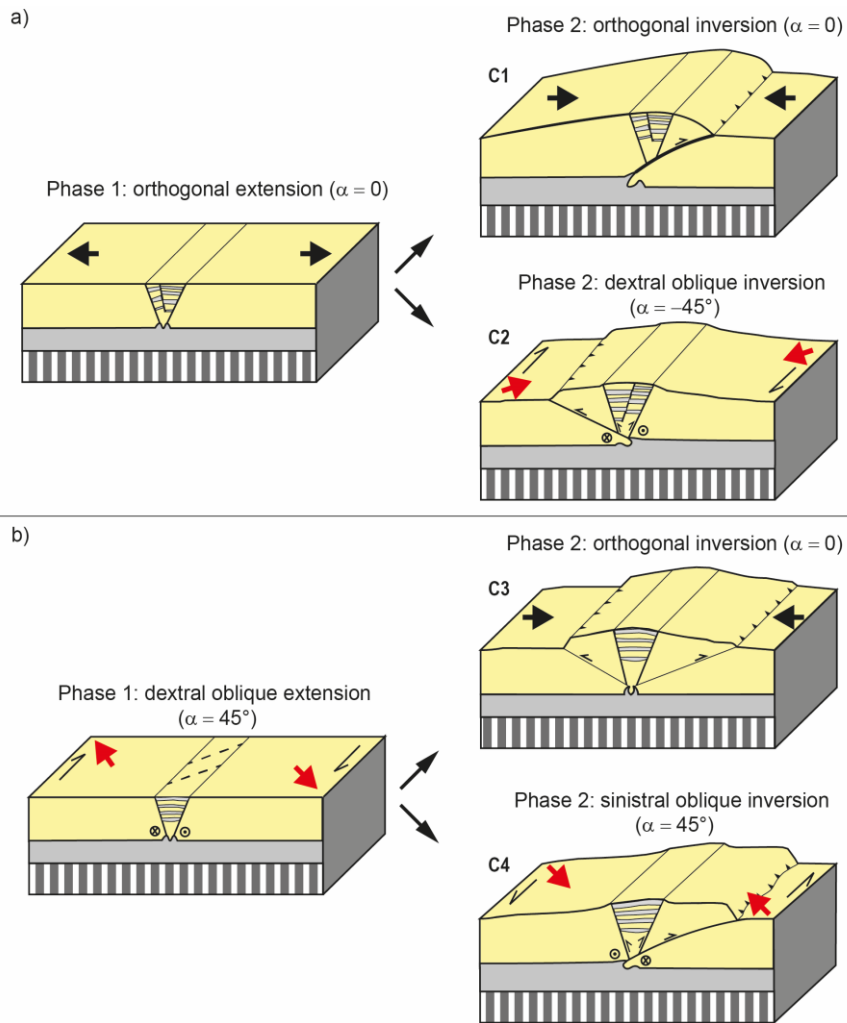


Figure 10: Schematic summary of our experimental results with syn-rift sedimentation

4.2 Comparing model results with the Araripe Basin

This study was inspired by the Late Jurassic/Early Cretaceous Araripe Basin in NE Brazil, which is presently situated at 1000 m above sea level (Assine, 2007). This elevation is due to post-rift inversion for which two ~~main-end-member~~ scenarios have been proposed (~~regional uplift or rift fault reactivation or regional uplift~~, Peulvast and Bétard, 2015, and Marques et al., 2014 and Peulvast and Bétard, 2015, respectively, Fig. 1). Here we ~~discuss-revisit~~ these scenarios in the context of our model results, ~~and propose a third, updated scenario for inversion in the Araripe Basin.~~

The uplift of the Araripe Basin infill as explained by the Peulvast and Bétard (2015) scenario involves a ~~large-scale rather than local basin inversion produced by regional tectonic uplift (Fig. 1). According to these authors, the present-day high standing mesa formation of the Araripe Basin is the result of differential erosion due to the presence of a strong sandstone formation covering the rift and post-rift sedimentary formations. However, other work demonstrates continuing ca. E-W compression across the South American plate (Assumpção, 1992; Coblenz and Richardson, 1996; Lima, 2003; Marques et al., 2013; Assumpção et al., 2016), combined with fault inversion in the region (e.g. Bezerra et al., 2020; Vasconcelos et al., 2021), suggesting that compressional horizontal stresses must have played a role in the inversion of the Araripe Basin as well.~~

Marques et al. (2014) proposed that inversion of the basin resulted from such regional horizontal compression acting on the South American plate due to the opening of the South Atlantic Ocean to the east (ridge-push) and the development of the Andes Cordillera to the west. Furthermore, Marques et al. (2014) ~~concluded that these combined forces stresses combined were the cause for reactivation and inversion of high angle normal faults.~~ Additionally, the authors stated that the obliquity of the normal faults in relation to the inversion stresses, in combination with fluid injection along the fault planes, facilitated fault reactivation. However, although we observed some fault reactivation in our oblique inversion models, this reactivation did never lead to full inversion of the graben normal faults (Figs. 9 and 10). In fact, no large-scale normal fault reactivation has been observed on seismic sections from the Araripe Basin (Ponte and Ponte-filho, 1996). Instead, Rosa et al. (2022) described limited reverse movement and fault inversion during Early Cretaceous rifting, when the basin changed from a system undergoing NE-SW extension to a system undergoing NW-SE extension. These authors reported positive flower structures on seismic lines that only affected syn-rift units, and suggested that the inversion of normal faults, which Marques et al. (2014) attributed to the most recent inversion of the Araripe basin, might in fact have occurred locally during the initial rifting phase instead. Furthermore, the post-rift sediments of the Araripe Basin cover an area larger than the extent of the original rift grabens and were deposited directly over the pre-Cambrian basement (Assine, 2007), and large-scale offset of these post-rift units is not observed in the field.

However, recent work shows that mild post-rift fault inversion did take place in the basin (Cardoso, 2010) and also other studies detected inversion in basins from the same rifting system the Araripe Basin is part of (e.g. Rio do Peixe Basin, Potiguar Basin, Bezerra et al., 2020; Vasconcelos et al., 2021). These authors analysed seismic data and described a mild to moderate inversion along the normal faults of these basins, although no full-scale basin inversion *sensu* Marques et al. (2014) was observed. Similar observations are

Formatted: Not Highlight

655 made on seismic sections from the Araripe Basin (Ponte and Ponte-filho, 1996), supporting the interpretation that horizontal shortening must have played a role in the inversion of the Araripe Basin. However, this shortening must have been accommodated in some other way than large-scale normal fault inversion. Marques et al. (2014) proposed that inversion of the basin resulted from a regional horizontal compression of the South American plate due to the opening of South Atlantic Ocean to the east (ridge-push) and the development of the Andes Cordillera to the west. Furthermore, Marques et al. (2014) concluded that these forces combined were the cause for reactivation and inversion of high angle normal faults. Additionally, the authors stated that the obliquity of the normal faults in relation to the inversion stresses was the facilitator for fault reactivation. However, although we observed some fault reactivation in our oblique inversion models, this reactivation did never lead to full inversion of the graben normal faults (Figs. 9 and 10), which contradicts the Marques et al. (2014) scenario. In fact, no large scale fault reactivation has been observed in the Araripe Basin (Ponte and Ponte filho, 1996). Rosa et al. (2022) described reverse movement and fault inversion during rifting phase in the Early Cretaceous, when the basin changed from an initial NE-oriented transtensional basin to a NW-oriented transtensional basin. Rosa et al. (2022) interpreted two Araripe Basin seismic lines showing positive flower structures affecting only rift phase unites and not propagating to the youngest post-rift units, that represents the basin high standing topography feature. These authors pointed out that, maybe, inverted faults attributed to the most recent compressional inversion of the Araripe basin might be related to early rift inversion of the main stress axis. Rosa et al. (2022) interpreted two Araripe Basin seismic lines showing positive flower structures affecting only rift phase unites and not propagating to the youngest post-rift units, that represents the basin high standing topography feature.

675 Our modelling results provide a solution to this apparent paradox, which involves the development of large-scale low-angle reverse faults during oblique convergence that take up most of the shortening, thus leading to basin uplift with some, but very limited, reactivation of the original rift structures (Fig. 11). Given the regional E-W shortening causing inversion of the Ararip Basin and the SW-NE orientation of the initial grabens (Fig. 1a), this oblique shortening was most likely of a dextral nature. Furthermore, our models suggest that initial rift kinematics did not have a strong impact on the later inversion structures, the right-stepping *en échelon* basin arrangement of the Araripe basin is similar to oblique rifting structure in our models (Figs. 1a, 5, 8-10), and suggests an initial sinistral oblique rifting phase due to roughly E-W extension. Our new oblique inversion scenario also explains the relatively undeformed uplift of the post-rift sediments and is in line with observations from the nearby Rio de Peixe Basin. In this basin, which is situated to the NE of the Araripe Basin and is part of the same rift trend, The post-rift sediments of the Araripe basin, cover an area larger then the rift grabens domain and was deposited directly over the pre-Cambrian basement (Assine, 2007). In section view (Fig. 1; Assine, 2007; Peulvast and Bétard, 2015), we can observe that the Araripe Basin topographic feature standing out from the basement around it is formed by the post-rift units, while rift units are leveled with the basement. Thus, if the normal faults major inversion is the sole responsible for the Araripe Basin uplift, as proposed by Marques et al. (2014), one would expect structural compartmentation along the standing out topographic feature (outside and inside

Formatted: Font: Italic

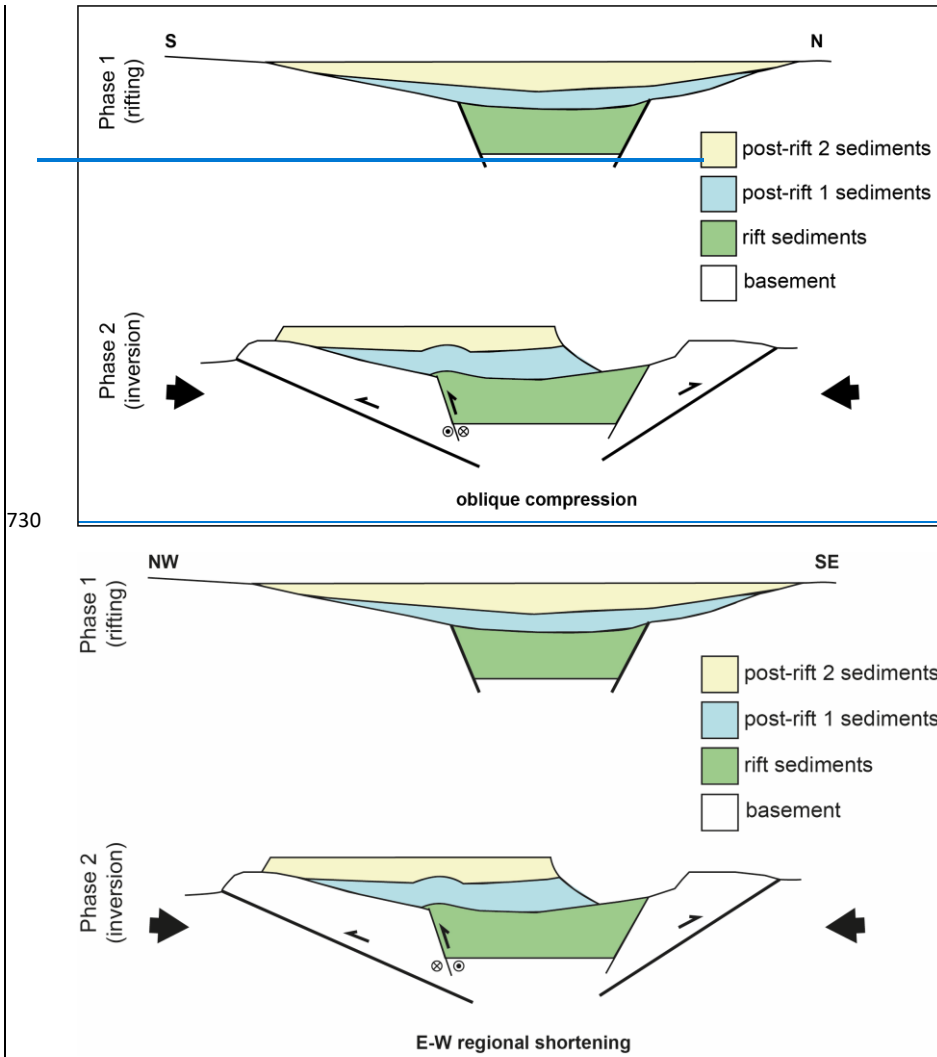
690 ~~the graben domain) and clear normal fault inversion in the seismic lines affecting post-rift units (Ponte and Ponte-filho, 1996; Rosa et al., 2022).~~

~~Immediately to the NE of the Araripe Basin, in the same rift trend. Vasconcelos et al. (2021) described mild to moderate inversion along the rift faults of the Rio do Peixe Basin. The main difference between these basins is the absence of post-rift units and no standing out topographic feature in the last one. The same, as well as authors even describe reverse faultings in the basement outside the graben area-. These observations of the Rio do Peixe Basin are in excellent agreement corroborating with our model results and we propose that s-forming new reverse faults outside the graben and mild reactivation of the normal faults.~~

~~A further argument against the Marques et al. (2014) scenario would be that the post-rift sediments outside the original graben domain would not have been uplifted in contrast to what we see in nature (Fig. 1).~~

700 ~~This basin uplift of post-rift sediments outside of the original graben domain can be explained by the Peulvast and Bétard (2015) scenario, who proposed a large scale topographic rather than local basin inversion produced by a regional tectonic uplift (Fig. 1). According to these authors, the present-day high standing-mesa formation of the Araripe Basin is the result of differential erosion due to the presence of a strong sandstone formation covering the rift and post-rift sedimentary formations. However, other work demonstrates the continuing compression across the South American plate (Assumpção, 1992; Coblenz and Richardson, 1996; Lima, 2003; Marques et al., 2013; Assumpção et al., 2016), combined with fault inversion in the region, and suggests that compressional horizontal stresses must have played a role in the Araripe Basin inversion. In fact, recent work shows that mild inversion did take place in the basin (Cardoso, 2010) and also other studies detected inversion in basins from the same rifting system as the Araripe Basin (e.g. Rio do Peixe Basin, Potiguar Basin, Bezerra et al., 2020; Vasconcelos et al., 2021). These authors analysed seismic data and described a mild to moderate tectonic reactivation inversion along the normal faults, however no full scale basin extrusion inversion is observed. Recent studies showed that lithospheric anomalies under the Araripe Basin could be responsible for the Borborema Province uplift (Garcia et al., 2019; Nemocón et al., 2021). This might imply that the basin went through a vertical push combined with horizontal compression (Garcia et al., 2019). We thus find that independently of any vertical forces acting on the lithosphere below the basin causing regional uplift, the horizontal compression affecting the South American plate is the main responsible for inversion of the Araripe Basin. We thus find that neither of the two end-member scenarios seems to fully explain the inversion observed in the Araripe Basin area.~~

715 ~~However, we propose an alternative scenario based on our analogue model results (Fig. 11). This scenario involves a basin-scale uplift facilitated by newly developed reverse faults rooted at the base of the original graben structure. At the same time, we only observed the mild inversion of the rift structures reactivation is shown to be only possible in oblique compression scenario when syn-rift sediments are present. As such this model same scenario involving can readily explain the field observations from the Araripe Basin as well. Furthermore, the inferred but also predicts the presence of large low-angle reverse faults (with a strike-slip component) outside the original rift basin as predicted by our models, which provides a strong incentive for further field investigations to verify this our proposed scenario for inversion in of the Araripe Basin.~~



730

735

Figure 11: Proposed tectonic evolution scenario for of the Araripe Basin inversion based on our analogue model results and data from literature. The scenario involves an initial rifting phase creating SW-NE oriented basins, followed by dextral oblique compression convergence due to general E-W oriented convergence. See text for details. Modified after Marques et al. (2014).

5 Conclusions

In this study we completed a series of new analogue modeling experiments aimed at evaluating the scenarios for basin inversion in the Araripe Basin in NE Brazil (~~full border fault reactivation vs. regional uplift~~). We tested the influence of orthogonal ($\alpha=0^\circ$) or oblique ($\alpha=45^\circ$) extension, followed by either orthogonal or oblique ~~compression~~ convergence on rift development and on subsequent inversion structures. We find that:

- During rifting without sedimentation, orthogonal ~~extension~~ divergence creates through-going border faults, whereas oblique ~~extension~~ divergence leads to the initial formation of ~~en-echelon~~ échelon faults that eventually will link up to establish large ~~border-graben boundary~~ faults. Rift basins with syn-rift sedimentation follow a similar evolution, however the sedimentary loading ~~causes increased~~ subsidence compared to models without sedimentation.
- During inversion, a major part of the deformation is accommodated by newly formed ~~low-low-angle~~ reverse faults. Within that framework, models without sedimentation saw significant intra-graben fault reactivation, roughly independent of inversion direction ($\alpha=0^\circ$ or $\alpha=45^\circ$ ~~orthogonal or oblique~~). By contrast, in models with syn-rift sedimentation, inversion caused only minor reactivation of the original ~~rift-graben boundary~~ faults during oblique ~~compression~~ convergence, due to the sedimentary infill acting as ~~a buffer during compression~~ a buffer. Orthogonal ~~compression~~ convergence in models with syn-rift sediments did not lead to rift fault reactivation.
- An assessment of the existing scenarios for inversion ~~in~~ of the Araripe basin with our model results as well as data from the field show that these scenarios do not fully explain all observations of the natural example. Therefore, based on our model results we propose an alternative scenario involving ~~dextral~~ oblique ~~compression~~ inversion and the development of ~~low-low-angle~~ reverse faults ~~(with a strike-slip component) outside the basin~~. This scenario ~~better explains the available field observations in the Araripe Basin but also provides and~~ incentive for future (field) studies.

765 Authors contributions

PCR, FZ and GS planned and designed the experiments. PCR completed the experiments, analysed the model results, and wrote the first manuscript draft. FZ participated in running some of the experiments. FZ and TCS helped performing the model analysis. PCR, FZ, GS, RSS, TCS participated in the interpretation of the model results, and reviewed and edited the manuscript.

770 Competing interests

The authors declare that they have no conflict of interest.

Acknowledgements

775 PCR and RSS gratefully acknowledge the support from research and development project “Correlação
estratigráfica, evolução paleoambiental e paleogeográfica e perspectivas exploratórias do Andar Alagoas”,
sponsored by Shell Brasil Petróleo Ltda, and the strategic importance of the support given by ANP (Brazil’s
National Oil, Natural Gas and Biofuels Agency) through the R&D levy regulation (Technical Cooperation
#20.219-2). PCR acknowledges CAPES – Coordination for the Improvement of Higher Education
780 Personnel – for their financial support. FZ and TCS were funded by the Swiss National Science Foundation
(via grant 200021-178731, <https://data.snf.ch/grants/grant/178731>, awarded to GS), which also covered the
Open Access publication costs. FZ was also funded by a GFZ Discovery Fund fellowship. RSS
acknowledges CNPq n° 311748/2018-0, FAPERJ n° E-26/200.995/2021 and Swiss National Science
Foundation n° IZSEZO_191196/1 (<https://data.snf.ch/grants/grant/191196>) research grants. We thank
785 Florian Ott and Kirsten Elger for helping us creating a GFZ data publication **containing supplementary
material (Richetti et al. in prep).** reviewers Fernando Ornelas Marques and Ioan Munteanu for their
constructive feedback, and editor Ernst Willingshofer for handling the review process.

Formatted: Highlight

Data availability

790 Detailed overviews of model results are ~~made~~ publicly available in the form of a GFZ data publication
(Richetti et al. in prep).

Temporary link: https://1drv.ms/u/s!AnD2tIs1Utsrg_8b10PsZiOu7qn1Yw?e=KLkOdi

Example of GFZ data publication: <https://doi.org/10.5880/fidgeo.2021.042>

References

- 795 Adam, J., Urai, J. L., Wieneke, B., Oncken, O., Pfeiffer, K., Kukowski, N., Lohrmann, J., Hoth, S., van der Zee, W., and Schmatz, J.: Shear localisation and strain distribution during tectonic faulting—new insights from granular-flow experiments and high-resolution optical image correlation techniques, *J Struct Geol*, 27, 283–301, <https://doi.org/10.1016/j.jsg.2004.08.008>, 2005.
- Assine, M. L.: Bacia do Araripe, *Boletim de Geociências da Petrobras*, 15, 371–389, 2007.
- 800 [Assumpcao, M.: The regional intraplate stress field in South America. *J Geophys Res*, 97, 11889. <https://doi.org/10.1029/91JB01590>, 1992.](#)
- [Assumpção, M., Dias, F. L., Zevallos, I., and Naliboff, J. B.: Intraplate stress field in South America from earthquake focal mechanisms. *J South Am Earth Sci*, 71, 278–295. <https://doi.org/10.1016/j.jsames.2016.07.005>, 2016.](#)
- 805 Bezerra, F. H., de Castro, D. L., Maia, R. P., Sousa, M. O. L., Moura-Lima, E. N., Rossetti, D. F., Bertotti, G., Souza, Z. S., and Nogueira, F. C. C.: Postrift stress field inversion in the Potiguar Basin, Brazil – Implications for petroleum systems and evolution of the equatorial margin of South America, *Mar Pet Geol*, 111, 88–104, <https://doi.org/10.1016/J.MARPETGEO.2019.08.001>, 2020.
- [Bonini, M., Sani, F., and Antonielli, B.: Basin inversion and contractional reactivation of inherited normal faults: A review based on previous and new experimental models. *Tectonophysics*, 522–523, 55–88. <https://doi.org/10.1016/j.tecto.2011.11.014>, 2012.](#)
- 810 Boutelier, D., Schrank, C., and Regenauer-Lieb, K.: 2-D finite displacements and strain from particle imaging velocimetry (PIV) analysis of tectonic analogue models with TecPIV, *Solid Earth*, 10, 1123–1139, <https://doi.org/10.5194/se-10-1123-2019>, 2019.
- 815 Brito Neves, B. B., Santos, E. J., and van Schmus, W. R.: Tectonic history of the Borborema province, northeastern Brazil, in: 31st International Geological Congress, 151–182, 2000.
- Broerse, T., Krstekanić, N., Kasbergen, C., and Willingshofer, E.: Mapping and classifying large deformation from digital imagery: application to analogue models of lithosphere deformation, *Geophys J Int*, 226, 984–1017, <https://doi.org/10.1093/gji/ggab120>, 2021.
- 820 Brun, J.-P. and Nalpas, T.: Graben inversion in nature and experiments, *Tectonics*, 15, 677–687, <https://doi.org/10.1029/95TC03853>, 1996.
- Buck, W. R.: Modes of continental lithospheric extension, *J Geophys Res Solid Earth*, 96, 20161–20178, <https://doi.org/10.1029/91JB01485>, 1991.
- Byerlee, J.: Friction of Rocks, in: *Rock Friction and Earthquake Prediction*, edited by: Byerlee, J. D. and Wye, M., Birkhäuser Basel, Basel, 615–626, https://doi.org/10.1007/978-3-0348-7182-2_4, 1978.
- 825 Camacho, C. R., Oliveira e Souza, F. R. F. R.: O arcabouço estrutural da Bacia Sedimentar do Araripe, Província Borborema, baseado em dados aeromagnetométricos, *Geol. USP, Série científica*, 17, 3, 149–161, <https://10.11606/issn.2316-9095.v17-393>, 20
- 830 Cardoso, F. M. C.: O graben da Palestina: contribuição à estratigrafia e estrutura do estágio rifte na Bacia do Araripe, Nordeste do Brasil, Universidade Federal do Rio Grande do Norte, Natal, 1–129 pp., 2010.
- [Coblentz, D. D. and Richardson, R. M.: Analysis of the South American intraplate stress field. *J Geophys Res Solid Earth*, 101, 8643–8657. <https://doi.org/10.1029/96JB00090>, 1996.](#)
- 835 di Domenica, A., Petricca, P., Trippetta, F., Carminati, E., and Calamita, F.: Investigating fault reactivation during multiple tectonic inversions through mechanical and numerical modeling: An application to the Central-Northern Apennines of Italy, *J Struct Geol*, 67, 167–185, <https://doi.org/10.1016/j.jsg.2014.07.018>, 2014.

Formatted: English (United Kingdom)

Field Code Changed

Formatted: English (United Kingdom)

- Dubois, A., Odonne, F., Massonnat, G., Lebourg, T., and Fabre, R.: Analogue modelling of fault reactivation: tectonic inversion and oblique remobilisation of grabens, *J Struct Geol*, 24, 1741–1752, [https://doi.org/10.1016/S0191-8141\(01\)00129-8](https://doi.org/10.1016/S0191-8141(01)00129-8), 2002.
- 840 Ganade de Araujo, C. E., Weinberg, R. F., and Cordani, U. G.: Extruding the Borborema Province (NE-Brazil): A two-stage Neoproterozoic collision process, *Terra Nova*, 26, 157–168, <https://doi.org/10.1111/ter.12084>, 2014.
- 845 [Guillaume, B., Gianni, G. M., Kermarrec, J.-J., and Bock, K.: Control of crustal strength, tectonic inheritance, and stretching/shortening rates on crustal deformation and basin reactivation: insights from laboratory models, *Solid Earth*, 13, 1393–1414, <https://doi.org/10.5194/se-13-1393-2022>, 2022.](#)
- [Gurgel, S. P. P., Bezerra, F. H. R., Corrêa, A. C. B., Marques, F. O., and Maia, R. P.: Cenozoic uplift and erosion of structural landforms in NE Brazil, *Geomorphology*, 186, 68–84, <https://doi.org/10.1016/j.geomorph.2012.12.023>, 2013.](#)
- 850 Hubbert, M. K.: Theory of scale models as applied to the study of geologic structures, *Geol Soc Am Bull*, 48, 1459–1520, <https://doi.org/10.1130/GSAB-48-1459>, 1937.
- Jara, P., Likerman, J., Charrier, R., Herrera, S., Pinto, L., Villarroel, M., and Winocur, D.: Closure type effects on the structural pattern of an inverted extensional basin of variable width: Results from analogue models, *J South Am Earth Sci*, 87, 157–173, <https://doi.org/10.1016/j.jsames.2017.10.018>, 2018.
- 855 Klinkmüller, M., Schreurs, G., Rosenau, M., and Kemnitz, H.: Properties of granular analogue model materials: A community wide survey, *Tectonophysics*, 684, 23–38, <https://doi.org/10.1016/j.tecto.2016.01.017>, 2016.
- Lamarque, G. and Julià, J.: Lithospheric and sub-lithospheric deformation under the Borborema Province of NE Brazil from receiver function harmonic stripping, *Solid Earth Discussions*, 1–20, <https://doi.org/10.5194/se-2019-41>, 2019.
- 860 Lima, C.: Ongoing compression across South American plate: observations, numerical modelling and some implications for petroleum geology, Geological Society, London, Special Publications, 209, 87–100, <https://doi.org/10.1144/GSL.SP.2003.209.01.09>, 2003.
- 865 Maestrelli, D., Montanari, D., Corti, G., del Ventisette, C., Moratti, G., and Bonini, M.: Exploring the Interactions Between Rift Propagation and Inherited Crustal Fabrics Through Experimental Modeling, *Tectonics*, 39, <https://doi.org/10.1029/2020TC006211>, 2020.
- [Marques, F. O. and Nogueira, C. R.: Normal fault inversion by orthogonal compression: Sandbox experiments with weak faults, *J Struct Geol*, 30, 761–766, <https://doi.org/10.1016/j.jsg.2008.02.015>, 2008.](#)
- 870 [Marques, F. O., Nikolaeva, K., Assumpção, M., Gerya, T. V., Bezerra, F. H. R., do Nascimento, A. F., and Ferreira, J. M.: Testing the influence of far-field topographic forcing on subduction initiation at a passive margin, *Tectonophysics*, 608, 517–524, <https://doi.org/10.1016/j.tecto.2013.08.035>, 2013.](#)
- Marques, F. O., Nogueira, F. C. C., Bezerra, F. H. R., and de Castro, D. L.: The Araripe Basin in NE Brazil: An intracontinental graben inverted to a high-standing horst, *Tectonophysics*, 630, 251–264, <https://doi.org/10.1016/j.tecto.2014.05.029>, 2014.
- 875 Marshak, S., Haq, S. S. B., and Sen, P.: Ramp initiation in fold-thrust belts: Insight from PIV analysis of sandbox models, *J Struct Geol*, 118, 308–323, <https://doi.org/10.1016/j.jsg.2018.11.006>, 2019.
- de Matos, R. M. D.: The Northeast Brazilian Rift System, *Tectonics*, 11, 766–791, <https://doi.org/10.1029/91TC03092>, 1992.
- 880 Molnar, N., Cruden, A., and Betts, P.: The role of inherited crustal and lithospheric architecture during the evolution of the Red Sea: Insights from three dimensional analogue experiments, *Earth Planet Sci Lett*, 544, 116377, <https://doi.org/10.1016/j.epsl.2020.116377>, 2020.

- Molnar, N. E., Cruden, A. R., and Betts, P. G.: Interactions between propagating rifts and linear weaknesses in the lower crust, *Geosphere*, 15, 1617–1640, <https://doi.org/10.1130/GES02119.1>, 2019.
- 885 Moulin, M., Aslanian, D., and Unternehr, P.: A new starting point for the South and Equatorial Atlantic Ocean, *Earth Sci Rev*, 98, 1–37, <https://doi.org/10.1016/j.earscirev.2009.08.001>, 2010.
- Mulugeta, G.: Squeeze box in a centrifuge, *Tectonophysics*, 148, 323–335, [https://doi.org/10.1016/0040-1951\(88\)90139-4](https://doi.org/10.1016/0040-1951(88)90139-4), 1988.
- 890 Nalpas, T., le Douaran, S., Brun, J. P., Unternehr, P., and Richert, J. P.: Inversion of the Broad Fourteens Basin (offshore Netherlands), a small-scale model investigation, *Sediment Geol*, 95, 237–250, [https://doi.org/10.1016/0037-0738\(94\)00113-9](https://doi.org/10.1016/0037-0738(94)00113-9), 1995.
- Neto, F. L. S., Julià, J., and Schimmel, M.: Upper-mantle structure of the Borborema Province, NE Brazil, from P-wave tomography: Implications for rheology and volcanism, *Geophys J Int*, 216, 231–250, <https://doi.org/10.1093/gji/ggy421>, 2019.
- 895 [Nogueira, F. C. C., Marques, F. O., Bezerra, F. H. R., de Castro, D. L., and Fuck, R. A.: Cretaceous intracontinental rifting and post-rift inversion in NE Brazil: Insights from the Rio do Peixe Basin, *Tectonophysics*, 644–645, 92–107, <https://doi.org/10.1016/j.tecto.2014.12.016>, 2015.](#)
- Panien, M., Schreurs, G., and Pfiffner, A.: Sandbox experiments on basin inversion: Testing the influence of basin orientation and basin fill, *J Struct Geol*, 27, 433–445, <https://doi.org/10.1016/j.jsg.2004.11.001>, 2005.
- 900 Panien, M., Schreurs, G., and Pfiffner, A.: Mechanical behaviour of granular materials used in analogue modelling: insights from grain characterisation, ring-shear tests and analogue experiments, *J Struct Geol*, 28, 1710–1724, <https://doi.org/10.1016/j.jsg.2006.05.004>, 2006.
- Peulvast, J. P. and Bétard, F.: A history of basin inversion, scarp retreat and shallow denudation: The Araripe basin as a keystone for understanding long-term landscape evolution in NE Brazil, *Geomorphology*, 233, 20–40, <https://doi.org/10.1016/j.geomorph.2014.10.009>, 2015.
- 905 Pinto, L., Muñoz, C., Nalpas, T., and Charrier, R.: Role of sedimentation during basin inversion in analogue modelling, *J Struct Geol*, 32, 554–565, <https://doi.org/10.1016/J.JSG.2010.03.001>, 2010a.
- Ramberg, H.: *Gravity, Deformation and the Earth's Crust*, Academic Press, London, 1981.
- 910 [Ramos, G. V., Vasconcelos, D. L., Marques, F. O., de Castro, D. L., Nogueira, F. C. C., Bezerra, F. H. R., Perez, Y. A. R., Souza, J. A. B., and Medeiros, V. C.: Relations between inherited basement fabric and fault nucleation in a continental setting: The Rio do Peixe Basin, NE Brazil, *Mar Pet Geol*, 139, 105635, <https://doi.org/10.1016/j.marpetgeo.2022.105635>, 2022.](#)
- Rebelo, T. B., Batezelli, A., and Luna, J. S.: Stratigraphic evolution and carbonate factory implications: Case study of the Albian carbonates of the Campos Basin, Brazil, *The Depositional Record*, 7, 271–293, <https://doi.org/10.1002/dep2.118>, 2021.
- 915 Richetti, P. C., Zwaan, F., Schreurs, G., Schmitt, R. S., Schmid, T. C.: Overviews and videos of top view imagery, topography data and DIC analysis results from analogue models of basin inversion. GFZ Data Services, in prep.
- 920 [Rosa, M. C., Morales, N., and Assine, M. L.: Transtensional tectonics during the Gondwana breakup in northeastern Brazil: Early Cretaceous paleostress inversion in the Araripe Basin, *Tectonophysics*, 846, 229666, <https://doi.org/10.1016/j.tecto.2022.229666>, 2023.](#)
- Schmid, T. C., Schreurs, G., and Adam, J.: Characteristics of continental rifting in rotational systems: New findings from spatiotemporal high resolution quantified crustal scale analogue models, *Tectonophysics*, 822, 229174, <https://doi.org/10.1016/J.TECTO.2021.229174>, 2022.
- 925 Schmid, T., Schreurs, G., Warsitzka, M., and Rosenau, M.: Effect of sieving height on density and friction of brittle analogue material: Ring-shear test data of quartz sand used for analogue experiments in the Tectonic Modelling Lab of the University of Bern, 2020.

- 930 [Schöfisch, T., Koyi, H., and Almqvist, B.: Magnetic Fabric Analyses of Basin Inversion: A Sandbox Modelling Approach, *EGUsphere*, 1–20, <https://doi.org/10.5194/egusphere-2022-1258>, 2022.](#)
- Schreurs, G. and Colletta, B.: Analogue modelling of faulting in zones of continental transpression and transtension, Geological Society, London, Special Publications, 135, 59–79, <https://doi.org/10.1144/GSL.SP.1998.135.01.05>, 1998.
- 935 Schreurs, G. and Colletta, B.: Analogue modelling of continental transpression, *Journal of the Virtual Explorer*, 07, <https://doi.org/10.3809/jvirtex.2002.00040>, 2002.
- Sibson, R. H. and Scott, J.: Stress/fault controls on the containment and release of overpressured fluids: Examples from gold-quartz vein systems in Juneau, Alaska; Victoria, Australia and Otago, New Zealand, *Ore Geol Rev*, 13, 293–306, [https://doi.org/10.1016/S0169-1368\(97\)00023-1](https://doi.org/10.1016/S0169-1368(97)00023-1), 1998.
- 940 Stanton, N., Ponte-Neto, C., Bijani, R., Masini, E., Fontes, S., and Flexor, J.-M.: A geophysical view of the Southeastern Brazilian margin at Santos Basin: Insights into rifting evolution, *J South Am Earth Sci*, 55, 141–154, <https://doi.org/10.1016/j.jsames.2014.07.003>, 2014.
- [Tron, V. and Brun, J.-P.: Experiments on oblique rifting in brittle-ductile systems, *Tectonophysics*, 188, 71–84, \[https://doi.org/10.1016/0040-1951\\(91\\)90315-J\]\(https://doi.org/10.1016/0040-1951\(91\)90315-J\), 1991.](#)
- 945 Turner, J. P. and Williams, G. A.: Sedimentary basin inversion and intra-plate shortening, *Earth Sci Rev*, 65, 277–304, <https://doi.org/10.1016/J.EARSCIREV.2003.10.002>, 2004.
- Vasconcelos, D. L., Marques, F. O., Nogueira, F. C. C., Perez, Y. A. R., Bezerra, F. H. R., Stohler, R. C., and Souza, J. A. B.: Tectonic inversion assessed by integration of geological and geophysical data: The intracontinental Rio do Peixe Basin, NE Brazil, *Basin Research*, 33, 705–728, <https://doi.org/10.1111/bre.12491>, 2021.
- 950 Vauchez, A., Neves, S., Caby, R., Corsini, M., Egydio-Silva, M., Arthaud, M., and Amaro, V.: The Borborema shear zone system, NE Brazil, *J South Am Earth Sci*, 8, 247–266, [https://doi.org/10.1016/0895-9811\(95\)00012-5](https://doi.org/10.1016/0895-9811(95)00012-5), 1995.
- del Ventisette, C., Montanari, D., Bonini, M., and Sani, F.: Positive fault inversion triggering “intrusive diapirism”: An analogue modelling perspective, *Terra Nova*, 17, 478–485, <https://doi.org/10.1111/j.1365-3121.2005.00637.x>, 2005.
- 955 del Ventisette, C., Montanari, D., Sani, F., and Bonini, M.: Basin inversion and fault reactivation in laboratory experiments, *J Struct Geol*, 28, 2067–2083, <https://doi.org/10.1016/J.JSG.2006.07.012>, 2006.
- Weijermars, R. and Schmeling, H.: Scaling of Newtonian and non-Newtonian fluid dynamics without inertia for quantitative modelling of rock flow due to gravity (including the concept of rheological similarity), *Physics of the Earth and Planetary Interiors*, 43, 316–330, [https://doi.org/10.1016/0031-9201\(86\)90021-X](https://doi.org/10.1016/0031-9201(86)90021-X), 1986.
- 960 Ziegler, P. A., Cloetingh, S., and van Wees, J.-D.: Dynamics of intra-plate compressional deformation: the Alpine foreland and other examples, *Tectonophysics*, 252, 7–59, [https://doi.org/10.1016/0040-1951\(95\)00102-6](https://doi.org/10.1016/0040-1951(95)00102-6), 1995.
- 965 Zwaan, F. and Schreurs, G.: How oblique extension and structural inheritance influence rift segment interaction: Insights from 4D analog models, *Interpretation*, 5, SD119–SD138, <https://doi.org/10.1190/INT-2016-0063.1>, 2016.
- Zwaan, F. and Schreurs, G.: How oblique extension and structural inheritance influence rift segment interaction: Insights from 4D analog models, *Interpretation*, 5, SD119–SD138, <https://doi.org/10.1190/INT-2016-0063.1>, 2017.
- 970 [Zwaan, F., Chenin, P., Erratt, D., Manatschal, G., and Schreurs, G.: Competition between 3D structural inheritance and kinematics during rifting: Insights from analogue models, *Basin Research*, 34, 824–854, <https://doi.org/10.1111/bre.12642>, 2022a.](#)

975 Zwaan, F., Schreurs, G., Naliboff, J., and Buitter, S. J. H.: Insights into the effects of oblique extension on continental rift interaction from 3D analogue and numerical models, *Tectonophysics*, 693, 239–260, <https://doi.org/10.1016/j.tecto.2016.02.036>, 2016.

980 Zwaan, F., Schreurs, G., and Adam, J.: Effects of sedimentation on rift segment evolution and rift interaction in orthogonal and oblique extensional settings: Insights from analogue models analysed with 4D X-ray computed tomography and digital volume correlation techniques, *Glob Planet Change*, 171, 110–133, <https://doi.org/10.1016/j.gloplacha.2017.11.002>, 2018a.

Zwaan, F., Schreurs, G., Ritter, M., Santimano, T., and Rosenau, M.: Rheology of PDMS-corundum sand mixtures from the Tectonic Modelling Lab of the University of Bern (CH), *GFZ Data Services*, 1, 2018b.

985 Zwaan, F., Schreurs, G., and Rosenau, M.: Rift propagation in rotational versus orthogonal extension: Insights from 4D analogue models, *J Struct Geol*, 135, 103946, <https://doi.org/10.1016/J.JSG.2019.103946>, 2020.

[Zwaan, F., Schreurs, G., Buitter, S. J. H., Ferrer, O., Reitano, R., Rudolf, M., and Willingshofer, E.: Analogue modelling of basin inversion: a review and future perspectives, *Solid Earth*, 13, 1859–1905, <https://doi.org/10.5194/se-13-1859-2022>, 2022b.](https://doi.org/10.5194/se-13-1859-2022)

990 [Zwaan, F., Schreurs, G., Buitter, S., Ferrer, O., Reitano, R., Rudolf, M., and Willingshofer, E.: Analogue modelling of basin inversion: a review and future perspectives, *Solid Earth Discussions*, 2022, 1–84, <https://doi.org/10.5194/se-2022-8>, 2022.](https://doi.org/10.5194/se-2022-8)
[Zwaan, F., Schreurs, G., Rudolf, M., and Rosenau, M.: Ring-shear test data of feldspar sand FS900S used in the Tectonic Modelling Laboratory at the University of Bern \(Switzerland\), *GFZ Data Services*, <https://doi.org/10.5880/figeo.2022.008>, 2022c.](https://doi.org/10.5880/figeo.2022.008)

995

Formatted: English (United States)

Formatted: English (United States)

Formatted: Hyperlink, Font: (Default) +Body (Calibri), 11 pt, English (United States)

Field Code Changed